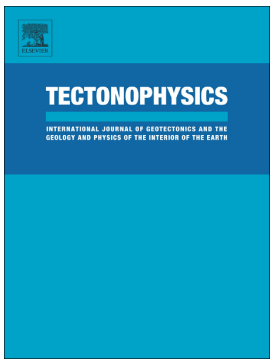

Sensitivity of gravity and topography regressions to earth and planetary structures

Pivetta Tommaso, Braitenberg Carla

PII: S0040-1951(19)30414-7

DOI: https://doi.org/10.1016/j.tecto.2019.228299

Reference: TECTO 228299

To appear in: *Tectonophysics*

Received date: 2 May 2019

Revised date: 17 October 2019

Accepted date: 21 November 2019

Please cite this article as: P. Tommaso and B. Carla, Sensitivity of gravity and topography regressions to earth and planetary structures, *Tectonophysics*(2019), https://doi.org/10.1016/j.tecto.2019.228299

Sensitivity of gravity and topography regressions to earth and planetary structures

Pivetta Tommaso and Braitenberg Carla*

Department of Mathematics and Geosciences, University of Trieste, Via Weiss 1, Trieste

*Corresponding author: berg@units.it

Abstract

The availability of global gravity fields and topography through calculation services like the International Centre for Global Earth Models, allows easy access to gravity data, greatly enlarging the spectrum of users. The applications extend much farther than the classic modeling through the gravity-specialist. We investigate the sensitivity of the joint analysis of topography and gravity data based on linear regression analysis and clustering of the response to particular characteristics of the lithosphere structure. The parameters of the regression analysis are predicted to have characteristic values, which allow to distinguish continental crust from oceanic crust, and signalize the presence of crustal inhomogeneity. Predictions are made through theoretical considerations and on synthetic models. We use the South Atlantic Ocean and the confining South American and African continents for illustration, where the regression parameters distinguish oceanic crust from the ridge up to the bathymetric inflection point, from the transitional crust and the continental crust, allowing to map these units. The general properties of the parameters are statistically relevant, since the errors on the parameters are less than 10% the amplitude of the parameters. We compare the regression parameters with those produced by a global crustal model (CRUST1.0), and find good correspondence between the observed and predicted fields. The analysis can be applied with machine learning algorithms, without the need of specific forward or inverse gravity modeling skills. It is therefore particularly useful in view of the enhanced access to the data through the calculation service, and could be implanted as an add-on tool, since it allows to efficiently distinguish isostatic contribution to the gravity field from crustal sources. Given the experience on the gravity field of the Earth, the analysis can be analogously extended to other planets. For illustration, we show that for Mars a coherent class of Martian crust can be identified.

Keywords: Global gravity field, Topography, Isostasy, Crustal units, Planets, Mars

1 Introduction

Gravimetry is experiencing an unprecedented boost thanks to the new possibilities offered by the satellite gravity missions that have been launched over the last 15 years. The ability to explore new areas, overcoming the obvious logistic problems of terrestrial gravity measurements, and to recover also temporal variations of the gravity field occurring at regional scales are the most interesting and intriguing features offered by these new tools. With the GOCE datasets we could have a look at large areas, with precision and spatial resolution adequate also for geological exploration: many interesting tectonic structures have been explored and also cross-continent correlation analysis between geological structures is now possible (Braitenberg, 2015; Ebbing et al., 2018). Also efforts in recovering the thermal structure from gravity has been recently made (Pastorutti and Braitenberg, 2019). Gravity data needs, as other geophysical observations, to be prepared in order to decompose the gravity field into signals attributable to different sources. Starting from the Free-air anomaly map, in which the normal field has been subtracted, the typical workflow involves the computation of the Complete Bouguer anomalies, in which the gravity effect of the superficial topography is removed from the original anomaly data. Bouguer anomalies are connected to the underground density distributions and typically are dominated by long-wavelength signals due to Moho undulations. These signals show high correlation with the topography in accordance to the isostatic theory. Other anomalies, usually non-correlated to topography, are present and are caused by lateral and vertical density inhomogeneities.

Many isostatic models have been proposed in the past years, incorporating more and more sophisticated physical models, in order to explain and remove the isostatic effect and enhance sub-superficial density variations. These models usually require an a priori knowledge of many physical parameters of the lithosphere, as the thermal state or the elastic parameters.

For remote and scarcely studied areas not all these parameters are available and in many cases some of them are also directly estimated by the gravity data itself, exploiting spectral properties of the field, as in the case of elastic parameters derived from admittance and coherence attributes of topography and gravity (Watts, 2001).

Statistical evaluation of the correlation between gravity and topographic fields has been proposed recently by (Braitenberg, 2015; Braitenberg et al., 2013) for studying the isostatic state of the lithosphere and detrending gravity data of satellite GOCE from the expected Moho contribution. The assumptions behind the method invoke a linear relation between Bouguer gravity field and the topography when the appropriate frequency bands are used, in accordance to isostatic models. The method, which performs a linear regression between suitably bandpass filtered topography and gravity, is useful as it is aparametric and because it allows to rapidly filter the isostatic contribution from the gravity data. Large areas, as those derived from GOCE satellite model, could be efficiently analyzed through this tool as proved from Africa and Europe examples. The method seems also promising as a tool to explore the underground structures of

other planets, as usually the first observations available for other extraterrestrial bodies are mainly global gravity field and topographic models. Examples are for instance the Earth's Moon (Wirnsberger et al., 2019; Zhao et al., 2019), Venus (Zampa et al., 2018) and Mars (Genova et al., 2016) where complete gravity and topography models are offered respectively up to d/o 420, 180 and 120.

The data can be analyzed in square windows, in each of them the regression is computed; the regression coefficients and their spatial distribution are related to the isostatic state and/or the presence of crustal density anomalies.

The analysis has proved to efficiently isolate the density inhomogeneities also on Free air data: in this case the relation between gravity and topography is positive albeit the modulus of the slope value is lower than the Bouguer case. This small positive relation is due to the fact that topographic masses are closer to the measurement point with respect to the Moho interface that should theoretically counterbalance the topographic effect. Also the uncompensated topography in the upper spectral band contributes to enforce this small positive relation.

Up to now, a detailed sensitivity test on controlled synthetic models using this method has not been carried out and the effects of the assumption, on the residualization process, of a linear relation between topography and gravity data have to be estimated yet. Different isostatic compensation mechanisms due to flexural models that cause alteration of the regression line still have to be considered and discussed. The effects on the regression parameters of lateral density changes in the crust have to be investigated and finally the pretreatment of the topography, in particular the choice of the bandpass filter frequencies must be examined further.

In this contribution we study the influence of all these important aspects on the regression analysis with the aim to explore the potentiality of this tool and assess its limits. Using crust and lithosphere models we explore the sensitivity of the regression analysis to different geodynamic scenarios. The method is presented and discussed first theoretically and then with applications in a terrestrial area that includes the Central Atlantic Ocean, South America and West Africa and then on an extraterrestrial planet (Mars). The linear relation between topography and gravity in the Airy case is analyzed in the first section, with a focus on the importance of pretreatment of the topography. Then flexural responses and density inhomogeneities are considered and discussed in the following sections. We focus in particular on the geophysical interpretation of the regression parameters and the derived residual maps.

2 Theoretical background

In this section we discuss the principal aspects of the regression analysis. Starting from a simple isostatic model which shows the main features of the method, we then introduce step by step more complex models, in order to predict the response of the regression parameters to different compensation mechanisms, as flexure, and density inhomogeneities.

2.1 Airy isostasy

To explore the regression analysis between Bouguer (or Free air) and topography we start considering the gravity effect of a simple crustal isostatic model as reported in figure 1.

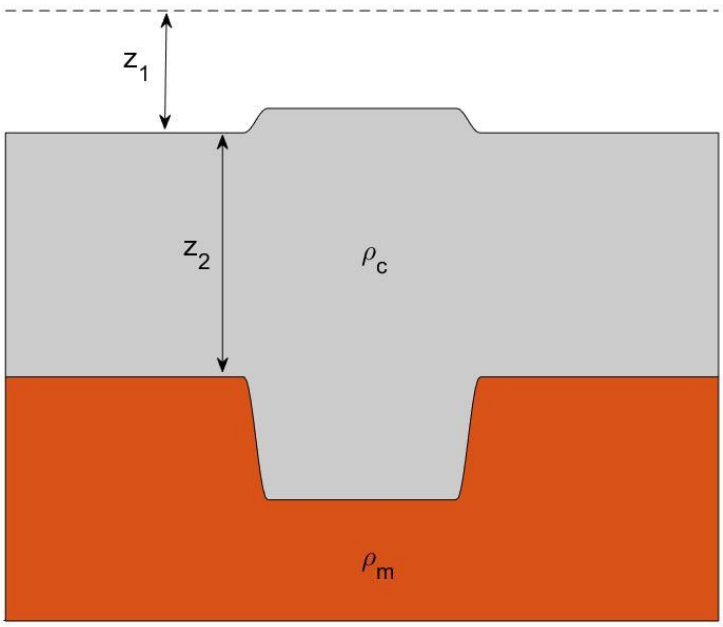

Figure 1. Sketch of the crustal model discussed in the following sections: z_1 represents the height of observation of the gravity anomalies; z_2 the reference depth of the Moho interface. ρ_c and ρ_m are respectively the crustal and mantle densities.

The gravity effect of this crustal model could be expressed as the sum of the topographic (Δgt) and of the crustal root (Δgc) effects.

Exploiting Parker expansion (Watts, 2001), truncated at the first order, we could approximate the two gravity effects according to the following expressions:

$$\Delta gc(k) = -2\,\pi\,G\,\Delta\rho\,e^{-k(z_1+z_2)}\,W(k) \qquad (1)$$

$$\Delta gt(k) = 2\,\pi\,G\,\rho_c\,e^{-kz1}\,H(k) \qquad (2)$$

With $z_1$the height of calculation of the anomalies above the topography, z_2 the reference depth of the Moho surface; Δρ is the density contrast between crust (ρ_c) and mantle (ρ_m), $H(k)$ is the Fourier transform of the topography while $W(k)$ the Fourier transform of the Airy Moho boundary defined as follows (Watts, 2001):

$$W(k) = -H(k)\frac{\rho_c}{\rho_m - \rho_c} \quad (3)$$

The sum of equations 1 and 2 gives an approximation in the frequency domain of the Free-air anomaly of our crustal model; the Bouguer field is obtained by subtracting from the Free-air field the topographic effect. The following equations report the Free air and Bouguer fields approximated with Parker expansion truncated at the first order:

$$\Delta gFA(k) = 2\,\pi\,G\,\rho_c\,e^{-kz_1}\,H(k) - 2\,\pi\,G\,\rho_c\,e^{-k(z_1+z_2)}\,H(k) \quad (4)$$

$$\Delta gBG(k) = -2\,\pi\,G\,\rho_c\,e^{-k(z_1+z_2)}\,H(k) \quad (5)$$

The first eq. shows the presence of two competing gravity effects that tend to cancel out each other leading to no correlation between topography and gravity. Equation 5 shows that there is a linear relation between the observed Bouguer field and a suitably filtered topography. The filter $e^{-k(z_1+z_2)}$, known also as Earth filter (Blakely, 1995), acts as a low pass filter with a cutoff-wavelength depending on the observation height (z_1) and on the reference depth of the Moho (z_2).

Dividing equations 4 and 5 by the Fourier Transform of the topography $H(k)$ we obtain the admittance curves plotted in Figure 2a; solid line is relative to admittance for Free-air, dashed line for Bouguer. The admittance curve reports, as a function of frequency, the value of the ratio of Bouguer (or Free-air) over Topography; this ratio corresponds to the slope of the regression line in the spatial domain. For this reason, it is interesting to investigate in detail the frequency dependence of these curves. The curves are calculated assuming typical crustal parameters for ρ_c = 2750 kg/m^3 and z_2 = 30000 m, while z_1 is set 5000 m.

At very low frequencies, we notice a zero correlation between topography and Free air gravity anomalies, as we expect from the isostatic theory. Airy isostasy predicts a strong anti-correlation between topography and the Bouguer field, which is effectively observed in figure 2a up to about 10^{-6} 1/m. In this range of frequencies the slope value approaches the simple Bouguer gradient $-2\,\pi\,G\,\rho_c = -0.1132$ mGal/m.

At low-mid frequencies (from 10^{-6} to 10^{-5} 1/m) we observe a positive slope up to a value of 0.07 mGal/m for Free-air anomalies, while the Bouguer admittance shows again negative values but with lower magnitude of the slope as frequency increases. At high frequencies (> 10^{-4} 1/m) both Free air and Bouguer tend to a zero value for the admittance. This discussion shows that if we perform the regression analysis between topography and Bouguer we expect different values of slope as a function of the frequency content of

topography; considering the regression between a suitably filtered topography and the Bouguer we expect to attenuate this frequency dependence.

A synthetic crustal model is presented herein to point out this aspect, showing also the differences that arise when considering the 'earth filtered' topography in the regression analysis. The model is composed by two synthetic topographies constituted by sine waves at two different frequencies (500 km and 1000 km) and by a crustal root that compensates the topographic load through an Airy mechanism. From this model we calculate the Bouguer anomaly and perform the regression analysis (figure 2b) on raw topography (crosses) and filtered topography (dots). For the regression analysis, the topography has been filtered applying the Earth filter ($e^{-k(z_1+z_2)}$) reported in equation 5, which acts as a low pass filter. The employed filter parameters were: z_1=30000 m, the average Moho depth, and z_2 = 5000 m, the observation height.

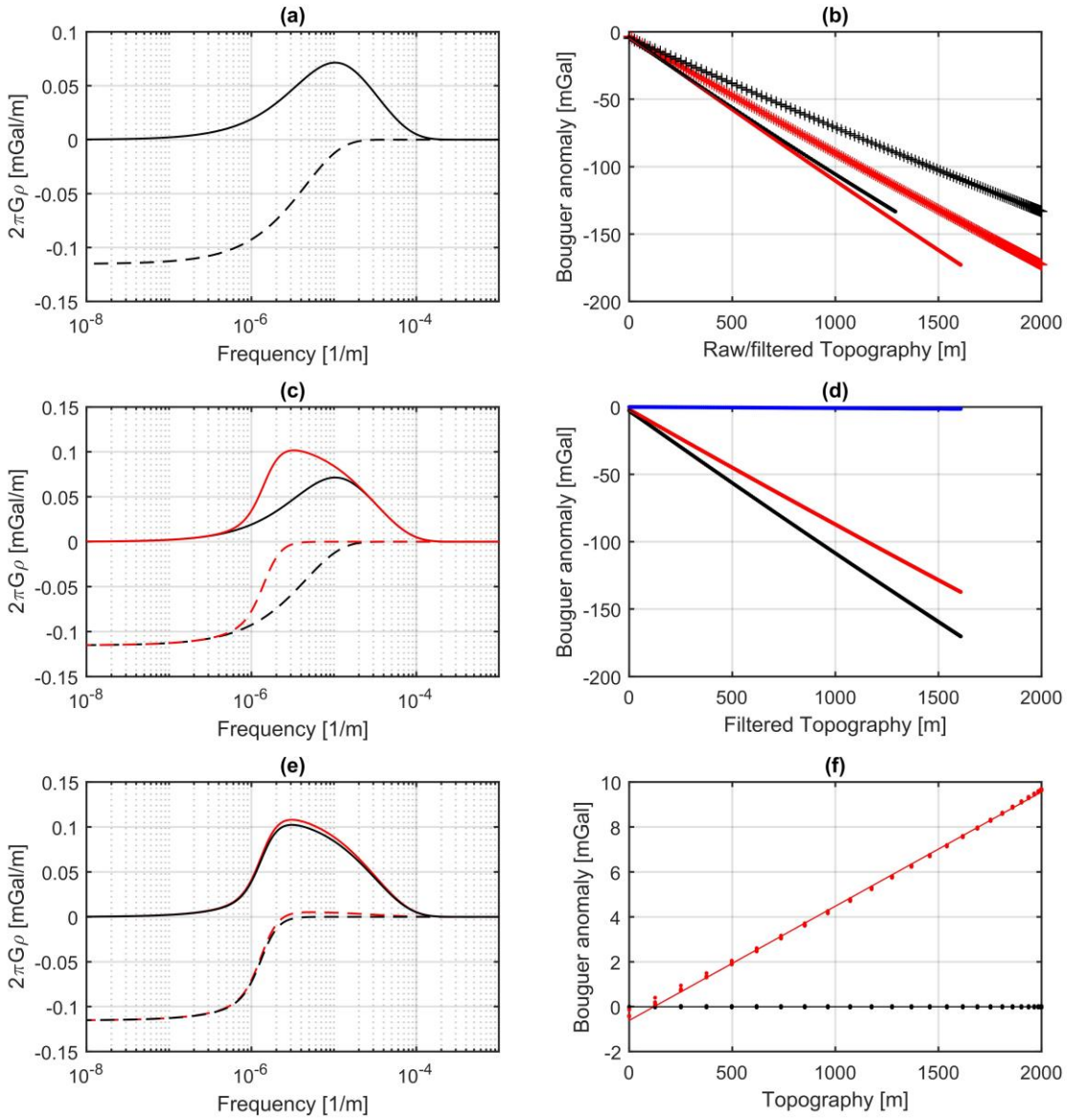

Figure 2, a) Admittance curves between Free air anomaly (solid line), Bouguer fields (stippled line) and topography for Airy isostasy. b) Regression between Bouguer and raw/filtered topography; raw topography has single spectral component with 500 km or 1000 km wavelength (respectively red and black crosses); red and black dots report the regression with appropriately filtered topographies. c) Free air (solid lines) and Bouguer (stippled lines) admittances for Airy (black) and flexural (red) cases. d) Regression between Bouguer and filtered topography for Airy (black) and flexure (red). Blue line regression with crustal model with infinite flexural rigidity. e) Free air and Bouguer admittance curves (respectively solid and stippled lines) for a crustal model with dense topography (red lines). Admittances for reference crust reported with black lines. f) Regression between Bouguer and topography for reference and dense crustal models. In this case the topography has 50 km wavelength.

The black lines are relative to the 500 km wavelength single spectral component topography; red lines refer to a longer single wavelength topography of 1000 km. We observe that the difference between the regression coefficients of the two topographies is widely reduced by considering a filtered topography. The

regression coefficient varies, in the case of non filtered topography, from -0.0843 mGal/m up to -0.06396 mGal/m, while for filtered topography the difference in the linear coefficients is reduced from -0.1036 up to -0.0982 mGal/m. These values are also closer to the theoretical linear coefficient $2\,\pi\,G\,\rho c$ that, for a homogeneous crust with density of 2750 kg/m^3, is equal to -0.1132 mGal/m.

2.2 Flexural effects

The flexure theory treats the crust and mantle as a filter to topographic loads, predicting that the Moho compensates in an Airy sense only the loads larger than a certain spatial extension (wavelength), while high frequency topographic loads are sustained by the rigidity of the plate.

In the frequency domain, the flexure response to a load is described by the following expression (Watts, 2001):

$$Y(k) = -H(k)\frac{\rho_c}{\rho_m - \rho_c}\,\Phi(k) \qquad (6)$$

Where

$$\Phi(k) = \left[\frac{Dk^4}{(\rho_m - \rho_c)g} + 1\right]^{-1} \qquad (7)$$

Equation 6 demonstrates that the flexural response is simply the Airy response filtered by the function $\Phi(k)$ which includes the physical characteristics of the plate, as the flexural rigidity D and the density contrast and g the average gravity value 9.81 m/s^2 (Watts, 2001).

Equations 4 and 5, considering the flexural effects become:

$$\Delta gFA(k) = 2\,\pi\,G\,\rho_c\,e^{-kz_1}\,H(k) - 2\,\pi\,G\,\rho_c\,e^{-k(z_1+z_2)}\,H(k)\Phi(k) \qquad (8)$$

$$\Delta gB(k) = -2\,\pi\,G\,\rho_c\,e^{-k(z_1+z_2)}\,H(k)\Phi(k) \qquad (9)$$

Similar to the previous example, we could calculate and plot the admittance curves in order to inspect the regression coefficient behavior as a function of frequency.

Figure 2c shows the Free Air and Bouguer admittances, respectively plotted with solid and dashed lines, for Airy (black) and flexural (red) isostatic compensation mechanisms. We considered a rigid crust, with an elastic thickness (*Te*) value of almost 90 km (D=6.5 10^{24} Nm). Flexure mechanism is responsible of increasing the correlation between topography and Free-air in the spectral band between 10^{-6} 1/m and 10^{-5} 1/m, while on the Bouguer field we observe a reduction of the correlation in this spectral band.

The comparison between Airy and flexure models in the frequency band 10^{-6} up to $3*10^{-6}$ shows higher admittance values for the Airy compensation; hence, the regression slope is affected by the compensation mechanism.

In figure 2d the two regression lines for both Airy and flexure mechanisms are plotted with the color code as in the previous figure; the topographies are constituted by a sine wave of 1000 km wavelength and for the regression analysis have been filtered with the $e^{-k(z_1+z_2)}$ filter, with z_2=30000 m and z_1=5000 m. As the rigidity of crust increases, we expect to observe less steep linear coefficients in the regression line; a limit case occurs where the rigidity of the crust sustains all the topographic loads, not causing crustal deflection and consequently reducing the observed Bouguer anomalies. The regression analysis here shows a zero slope (blue line in figure 2d).

2.3 Density inhomogeneities

The last aspect we investigate is the sensitivity of the regression analysis to density inhomogeneities. We consider a sine-wave topographic load with density ρ_{c2} = 2800 kg/m^3 and 100 km wavelength laying over a crust with density ρ_c = 2750 kg/m^3 and flexural rigidity D = 10^{23} Nm. The reference crust, used for computing the gravity anomalies, has a reference density equal to ρ_c. The Free air anomalies over the crustal model could be expressed according to eq.10 assuming Parker approximation truncated at the first term (Watts, 2001); Bouguer anomalies (eq. 11) are obtained by subtracting from the Free-air the topographic correction calculated with the reference density (ρ_c).

$$\Delta gFA(k) = 2\,\pi\,G\,\rho_{c2}\,e^{-kz_1}\,H(k) - 2\,\pi\,G\,(\rho_m - \rho_{c2})\,e^{-k(z_1+z_2)}\,H(k)\Phi(k) \qquad (10)$$

$$\Delta gB(k) = 2\,\pi\,G\,(\rho_{c2} - \rho_c)\,e^{-kz_1}\,H(k) - 2\,\pi\,G\,\rho_{c2}\,e^{-k(z_1+z_2)}\,H(k)\Phi(k) \qquad (11)$$

Figure 2e reports the admittance curves: the homogenous density is shown with black lines while red lines plot the admittances for the model with denser topography. Regarding the free air anomalies over the denser model we observe higher values of the admittance in the spectral band 2 10^{-6} - 2 10^{-5} 1/m with respect to the reference model. This implies a steeper regression line with respect to a homogeneous crust.

The admittance curves of the Bouguer field show almost the same values at low frequency (< 10^{-6}) and high frequencies (> 10^{-4} 1/m), independently on the presence/absence of crustal inhomogeneities. As in the previous models at low frequencies we expect a strong anti-correlation in accordance with isostatic theory, while at high frequencies very low correlation is found. The intermediate frequency band shows a positive admittance implying a positive correlation also in the spatial domain. This positive correlation arises from the incorrect density used for topographic correction and such effect is similar to what has been already

studied by several authors (Caratori Tontini et al., 2007; Nettleton, 1939). In this case the positive correlation peaks up to 0.0052 mGal/m.

Figure 2f reports the cross-plot between topography and Bouguer with the respective regression lines: red line for high density topography, black for reference density. The topography has wavelength of 100 km. Black line shows the absence of correlation as expected from the admittances curve, red line shows on the other hand a positive correlation with slope of 0.0051 mGal/m.

It is tempting to interpret quantitatively this slope value in terms of mis-modelled density (difference between actual density and the density used for topographic correction) through the simple Bouguer approximation $2\,\pi\,G\,\Delta\rho$. The value 0.0051 mGal/m leads to a density difference of 120 kg/m^3 which is not too far from the actual difference (150 kg/m^3).

This discrepancy is probably due to the compensation effect of the Moho that slightly alters the coefficient. For an infinitely rigid crust we obtain exactly the slope value for $2\,\pi\,G\,150$ kg/m^3 = 0.063 mGal/m.

Up to now, we have analyzed the effects of the density inhomogeneities that correlate with topography. However, in general, this is not guaranteed; volcanic areas are a typical example where the crust is markedly heterogeneous, with the presence of localized dense bodies. In this case, the regression analysis could be useful to separate the isostatic effect from the 'geological effect', which causes small-scale density variations and consequently generates further gravity anomalies.

Figure 3a reports the regression analysis over a crustal model composed of a broad mountain (250 km wavelength) that reaches 2000 m height and that is compensated at 30 km depth by a flexural mechanism, assuming *Te* = 40 km (D=5.7 10^{23} Nm). A crustal inhomogeneity with spherical shape is located 2 km below the topography, with a density contrast of +300 kg/m^3, and it is assumed to be sustained by the high crustal rigidity. The radius of the intruded body is 4 km.

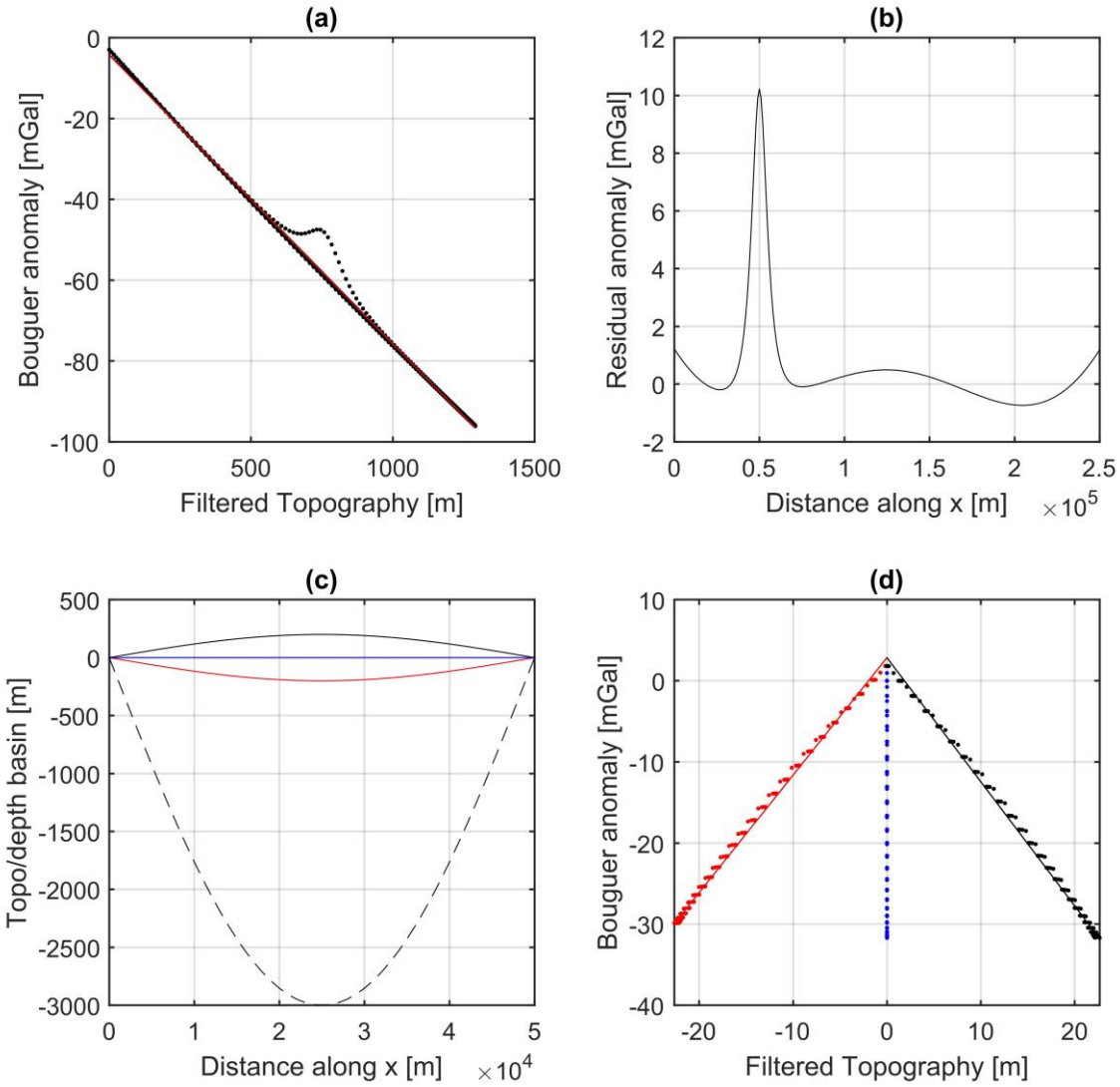

Figure 3. a) Regression between Bouguer and filtered topography. Bouguer field includes the effect of the isostatic compensation and of a crustal inhomogeneity uncorrelated with the topography. b) Residual map along a profile crossing the crustal inhomogeneity. c) Model of a synthetic sedimentary basin. Black line reports the upwelling topography; blue flat topography; red basin with topographic depression. Dashed line: sediment basement. d) Scatter plot of Bouguer and topography for a sedimentary basin. Red, blue and black coded as in Figure 3c.

We observe the regression line follows the isostatic long wavelength trend, and efficiently separates the effect of the crustal inhomogeneity. Figure 3b shows the residual anomaly g_{res} calculated as:

$$g_{res} = BG_{obs} - m\, h_{topo} - q \quad (12)$$

Here BG_{obs} is the observed Bouguer anomaly, sum of the compensation effect and the intrusion anomaly; m and q are the coefficients estimated by the regression analysis; h_{topo} is the filtered topography.

The last class we examine regarding density inhomogeneities investigates an alluvial plain and large scale sedimentary basins. These large structures are generally associated with moderate topographic reliefs and large negative gravity anomalies. What we expect from the regression analysis depends obviously on the basin topography: if the topography is a depression that has its minimum over the depocenter we expect a positive correlation in the regression line with very high values of slope. In case of flat topography, we expect a vertical asymptote in the cross-plot between topography and Bouguer. Figure 3c shows through a simple synthetic model three different cases: the dashed line indicates the basement's depth of the sedimentary basin which has a density contrast against crust of -200 kg/m^3; the three colored curves report three different topographies. Figure 3d shows the regression analysis with the anomalies due to the basin and the three topographies: the retrieved values of the coefficient are +/- 1.44 mGal/m for red and black lines (blue has a vertical asymptote) which are one magnitude higher with respect to the regression coefficients typical of the isostatic mechanism.

We highlight that observing such high values in the regression analysis, is a symptom for not observing the isostatic signal; hence, the analyst should be cautious in the interpretation of both the values of slope and the residual maps.

2.4 Pratt response

In oceanic areas, the model of compensation could be quite different from the continents; the important topographic variations in the bathymetry are usually compensated by lateral density variations induced by different thermal conditions in the mantle rather than by crustal thickness variations (Chappell and Kusznir, 2008). The crustal thickness in fact is almost constant and it is approximately 10 km.

We might wonder what could be the effect on the regression line of such compensation mechanism.

Again, we investigate the behavior of the regression line by inspecting the admittance curves. According to (Watts, 2001) the Free-air and Bouguer anomalies for a Pratt crustal model, which includes a rock-equivalent bathymetry $H(k)$ (Hirt et al., 2016), a crust of constant thickness tc and a mantle could be written as:

$$\Delta gFA(k) = 2\,\pi\,G\,\rho_c\,e^{-kz_1} + 2\,\pi\,G\,(\rho_m - \rho_c)e^{-k(t_c+z_1)}\,H(k) - 2\,\pi\,G\,(\rho_m)e^{-k(z_1+d-t_c)}\,H(k) \quad (13)$$

$$\Delta gB(k) = 2\,\pi\,G\,(\rho_m - \rho_{c2})\,e^{-kz_1} + 2\,\pi\,G\,(\rho_m - \rho_c)e^{-k(t_c+z_1)}\,H(k) - 2\,\pi\,G\,(\rho_m)e^{-k(z_1+d-t_c)}\,H(k) \quad (14)$$

where ρ_c is density of the oceanic crust, ρ_{c2} is the density used for the terrain correction, ρ_m the density of the mantle where topography=0 and d is the compensation depth.

For calculating the admittance curves we rely on the following typical parameters: ρ_c = 2900 kg/m^3, ρ_{c2} = 2750 kg/m^3, ρ_m = 3300 kg/m^3, z_1 = 5000 m, d = 120000 m and t_c = 10000 m.

Figure 4a shows for comparison the admittance curves for Bouguer and Free-air for the Airy model.

At very long wavelengths the Bouguer admittance strongly anticorrelates with topography for both Airy and Pratt; the value of the slope tends to the value $2\ \pi\ G\ \rho_{c2}$, where ρ_{c2} is the value used for the topographic correction. At higher frequencies, the two curves diverge, because our Pratt model compensates at deeper depths. Hence, in the spectral band 10^{-7} – 10^{-5} 1/m we could expect to observe differences in the regression slopes. The regression analysis over a synthetic crustal model composed by a topography with 1000 km wavelength is shown in figure 5c; the retrieved linear regression coefficients are respectively -0.058 mGal/m and -0.1038 mGal/m for Pratt and Airy cases. We observe also that the fit is worst at low topographic quotas for the Pratt model; this is due to the deeper compensation level of Pratt, which causes the appearance of long wavelength anomalies in the Bouguer field, which are uncorrelated to topography.

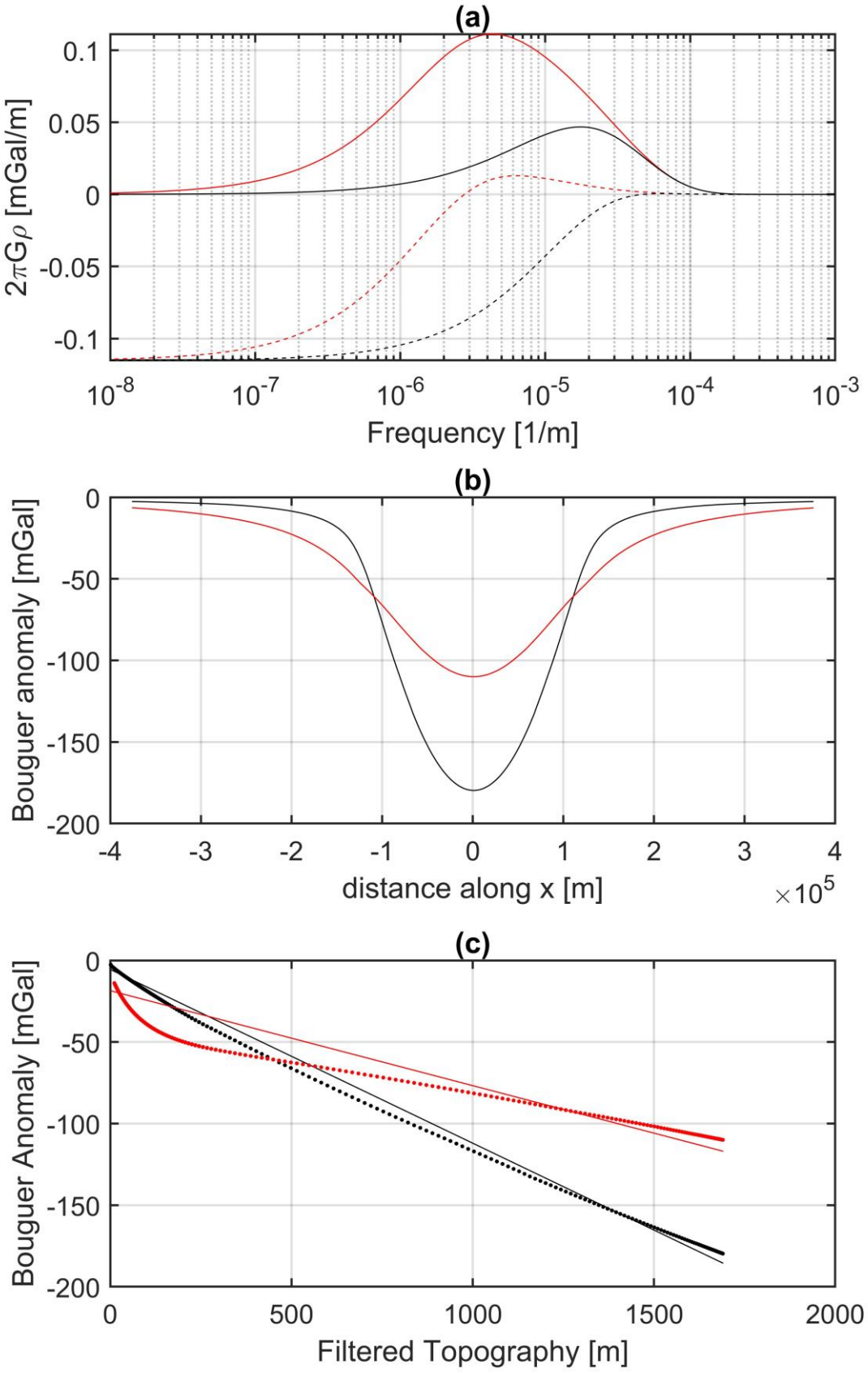
(a)
0.1
0.05
0
-0.05
-0.1
$2\pi G\rho$ [mGal/m]
10^{-8}
10^{-7}
10^{-6}
10^{-5}
10^{-4}
10^{-3}
Frequency [1/m]
(b)
0
-50
-100
-150
-200
Bouguer anomaly [mGal]
-4
-3
-2
-1
0
1
2
3
4
distance along x [m]
$\times 10^5$
(c)
0
-50
-100
-150
-200
Bouguer Anomaly [mGal]
0
500
1000
1500
2000
Filtered Topography [m]

Figure 4. a) Admittance curves between Free air anomaly (solid line), Bouguer fields (stippled line) and topography for Airy model (black) and Pratt model (red). b) Bouguer fields calculated for the Pratt model (red line) and Airy model (black line) c) Regression between Bouguer and filtered topography; red and black dots are relative to Pratt and Airy models respectively.

2.5 The intercept of the regression line

Up to now, we have considered only the slope of the regression line, not discussing the role of the intercept and its physical interpretation. In fact, all the above equations predict that for an isostatic model a zero value for the intercept should be found, which signifies that 0 m topography coincides with a 0 mGal anomaly.

A non-zero intercept implies a systematic shift of the anomalies, which could be physically explained for instance by a long wavelength anomaly related to density inhomogeneities in the mantle. Other possible causes are large sedimentary basins, i.e. Congo Basin, which is characterized by a marked negative gravity anomaly and a relatively flat topography over an area of almost $2\ 10^6$ km^2 (Braitenberg and Ebbing, 2009).

Practically a non-zero intercept is observed also over some of the synthetic models discussed above (figure 3a for instance). In this case, the value is very close to zero and in all the synthetics is less than 10 mGal; non-linear effects not considered in the regression analysis explain this discrepancy, with respect to the equations presented.

We expect to observe non-zero intercepts also in oceanic areas in particular where large abyssal plains show relatively flat topography for several hundreds of kilometers and the Bouguer anomalies are systematically high due to the removal of the bathymetric effect.

2.6 Residuals map

One of the interesting aspects in the regression analysis is the ability of the method to separate the gravity signals connected to the deep isostatic roots from the “geological effect” (inhomogeneities in the upper crust). The regression analysis assumes a linear relation between the Bouguer and an appropriately filtered topography; signals that fall outside the regression line are reported in the residual maps (Figure 3b).

However, the assumption of the linearity between Bouguer and topography should be further stressed since it would primarily impact the retrieved residuals map. We expect the non-linear effects to be more pronounced in proximity of steep topographies, such as at orogens or continental shelfs.

Figure 5 shows a simple synthetic test with the aim to illustrate the effect on the residualization of the linear approximation in the regression line. Figure 5a reports two crustal models over which the gravity

signals have been simulated: blue and yellow lines report the topographies of the two models while red and purple lines respectively the isostatic roots calculated assuming an Airy mechanism. The Bouguer fields for the two crusts are shown in figure 5c with the same color code as the roots in figure 5a. The regression analysis between the Bouguer and the filtered topographies are shown in figure 5b. We see that the model with the steep topography (blue dots) undulates around the linear fit, resulting in some artifacts at the edge of the orogeny in the residual maps (blue line in figure 5c). We emphasize that this residual has amplitudes lower than the 10% of the Bouguer anomalies and in general anomaly assumes values less than 30 mGals for an average 3000 m topography. The less steep topography produces smaller artifacts with residuals ranging in the interval +/-2 mGal.

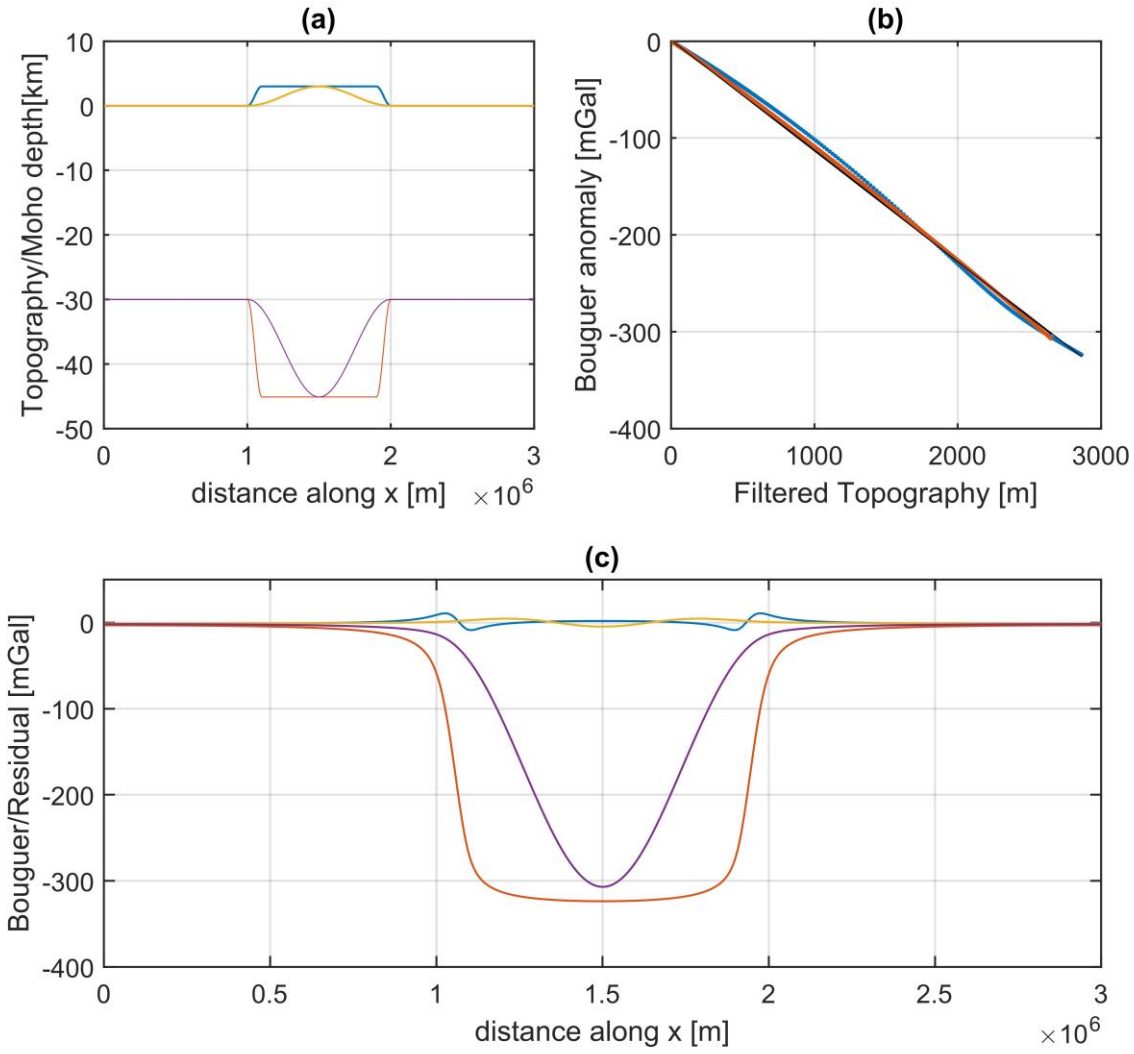

Figure 5. Synthetic models for testing the residualization. a) Topographies considered (blue and yellow) and their isostatic roots (red and purple). c) Bouguer fields (red and purple) of the two crustal models and residuals (blue and yellow) after the regression analysis. b) Regression between Bouguer and topography.

2.7 Discussion on the synthetics

The Regression analysis is apt to study the isostatic state of the crust and to separate the isostatic signal from the surface geologic contribution. The regression could be performed between the Bouguer field and a suitably filtered topography. The need for filtering is due to the decaying of the gravity with the quota of observation.

For a pure isostatic response, we expect a regression line with negative slope; variations in the linear coefficients could be due to different mechanisms of compensation and to the presence of systematic density variations in the crust: increasing the rigidity of the crust and/or the presence of a superficial dense topography produces less steep regression lines. Due to this bias a quantitative interpretation of the spatial variations of slope in terms of crustal density is complicated, not having at disposal other geophysical/geological constraints.

A positive correlation between Bouguer and topography is expected at high spatial frequencies over areas where dense rock formations outcrop. Large sedimentary basins with flat topographies are regions were the regression coefficients and the residuals should be treated with caution and are generally characterized by very high slope coefficients.

For regression in ocean areas we expect to observe again anticorrelation between Bouguer and the filtered topography; the compensation depth could influence the value of the slope of the regression line. Assuming a typical 120 km compensation depth, we should observe slightly less steep regression lines over the oceans with respect to continental areas.

Variations in the intercepts could be explained by long period density anomalies in the mantle, that systematically shift the anomalies at 0 m topography. However, non zero intercepts are also due to non-linear effects non accounted for in the simple linear regression approach.

3 Application of the regression analysis to the Central Atlantic area

We performed the regression analysis over the Central Atlantic area, including also the South America continental area and the African western sector. The topography and the gravity anomalies discussed herein, are all derived from global models offered as spherical harmonic expansions. GrafLab (Bucha and Janák, 2013) software was employed to synthetize the harmonic coefficients into a regular grid of 0.1° resolution at 10 km height.

Figure 6 reports the topography, the gravity disturbance, derived from the model EIGEN 6c4 (Förste et al., 2016), and the Bouguer anomaly of the investigated area. All the models have been developed up to degree and order (d/o) 720. The Bouguer field had been derived by correcting the gravity disturbance for the Earth2014 model (Rexer et al., 2016) which is a global model of the terrain attraction.

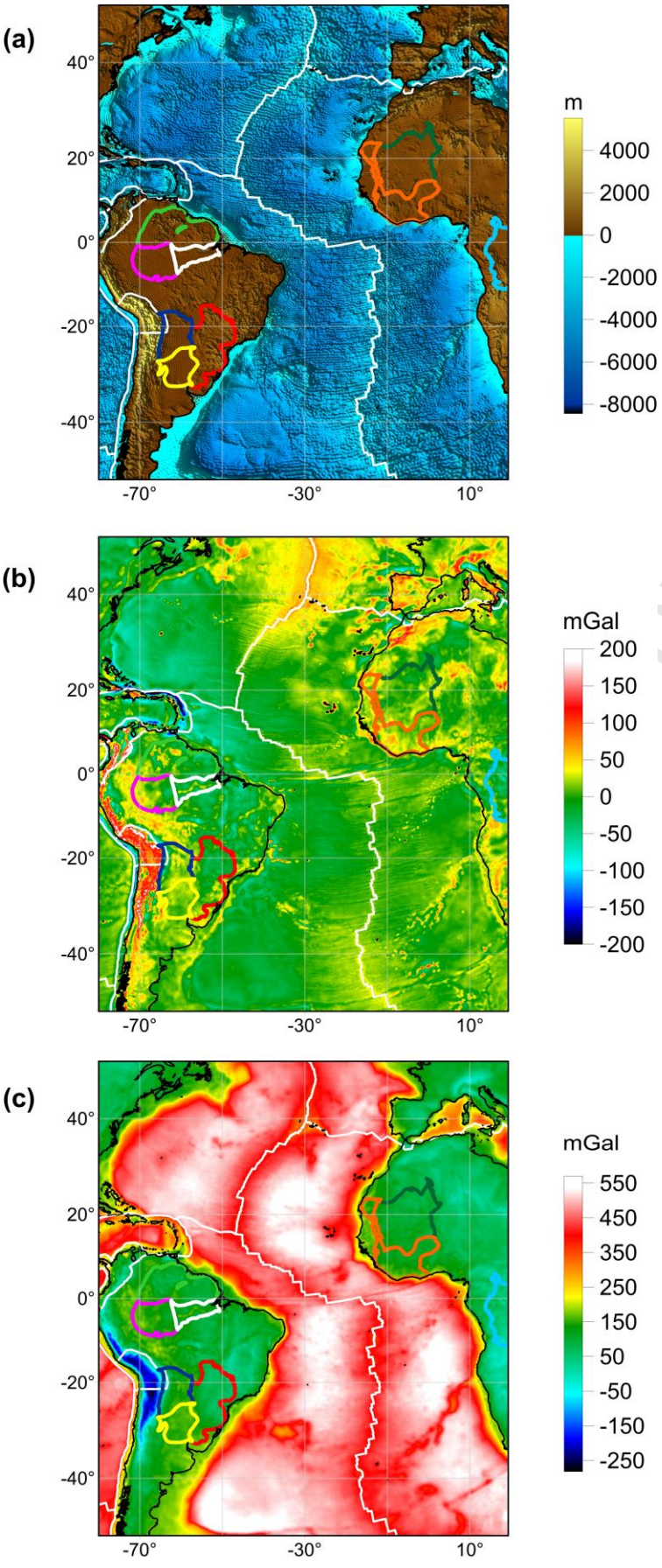
(a)
40°
20°
0°
-20°
-40°
-70°
-30°
10°
m
4000
2000
0
-2000
-4000
-6000
-8000
(b)
40°
20°
0°
-20°
-40°
-70°
-30°
10°
mGal
200
150
100
50
0
-50
-100
-150
-200
(c)
40°
20°
0°
-20°
-40°
-70°
-30°
10°
mGal
550
450
350
250
150
50
-50
-150
-250

Figure 6. a) Topography of the area from Etopo1 developed up to d/o 720. b) Gravity disturbance over the area from EIGEN-6c4 developed up to d/o 720. c) Bouguer anomaly derived from the correction of the gravity disturbance with the topographic effect from Earth2014 (Rexer et al., 2016)**. Selected geologic outlines from a USGS database** (Persits et al., 1997; Schenk et al., 1997) **are reported with various colors (description in text); the thin white line marks the Plate Boundaries after** (Coffin et al., 1998)**.**

The topography of the model developed up to d/o 720, which comprises also topographic features with wavelengths of 30-40 km, was further filtered before the regression analysis in order to account for the Earth filter (e^{-kz_2}) with z_2=40 km.

We perform the regression analysis on sliding windows, considering several different windows with areas of 2°x2°, 3°x3° and 7°x7°. In figure 7a,c slope and intercept maps are reported and refer to the analysis with the 3°x3° window; in general small windows tend to emphasize local features, hence the slope and intercept maps show large variations in the linear coefficients of the regression line. Large windows filter part of these high frequency variations and the coefficients are more stable; variations in the coefficients are due to large-scale differences in the crust and lithosphere. The comparison between different window sizes showed a general consistency of the retrieved spatial patterns of the regression coefficients; the 3°x3° window appeared a good compromise between the need of a sufficiently large window to detect the isostatic signals and the sensitivity to local variations in the regression coefficients.

Figure 7a reports the spatial variations of the slope of the regression line, while 7b shows the error on the regression coefficient, expressed in terms of standard error. Figure 7c and 7d report the intercept map and the residual maps; the residuals were calculated according to equation 12.

Comparing the slope, intercept and error maps in figure 7a, 7b 7c, we observe that all show a marked difference between the more recent and active areas (oceans) and the old continental areas composed by shields, cratons and intracratonic sedimentary basins. The old continental areas show slopes of the regression lines (Figure 7a) with a wide range of variability (+/-0.3 mGal/m) while oceanic areas are characterized by more stable linear coefficients. The errors (Figure 7b) on the linear regression coefficients are systematically higher over continents with respect to ocean. The intercept maps are consistent with the regression slopes map in terms of the spatial pattern, showing high values over ocean and lower values on inland. All these features signalize systematic differences in the structure of the two lithospheres with a more heterogeneous density structure over continental areas. In continental areas in fact, the tectonic processes have juxtaposed different crustal types over the past billion years, each characterized by different compositions, geometrical structure and physical properties.

Figure 7a reports the outlines of selected geologic provinces in South America and Africa, according to the USGS database (Persits et al., 1997; Schenk et al., 1997). We see that the geologic provinces can be distinguished by variations in the regression coefficients: for instance the Amazon basin (white outline) is

characterized by a steep negative regression line, in accordance to what we expect theoretically for a wide sedimentary basin. The Guyana shield (light green) is associated to very low slopes as well as the Paranà (red) and the Chaco (yellow) basins. The Solimoes basin (purple line) shows a very strong positive correlation, with slopes in the regression line exceeding 0.2 mGal/m.

The low slope values in the Guyana shield could be explained by the relatively high rigidity of the crust (*Te* > 50 km, (Tassara et al., 2007)), which is able to sustain most of the topographic reliefs present. The intracratonic Paranà basin is also associated to high values of *Te* (Tassara et al., 2007) and to the presence of a Large Igneous Province (Mariani et al., 2013); the combination of these phenomena could explain the relatively low values of the slope retrieved by our analysis.

Moving to west, the Andes show very stable regression coefficients with slope values close to -0.11 mGal/m as expected for an active orogeny characterized by deep crustal roots (Assumpção et al., 2013) and low *Te* values (Tassara et al., 2007). In the Chilean offshore, we observe that the boundary of the plate is marked by a narrow strip of positive slopes, probably linked to the peripheral bulge of the dense oceanic crust subjected to the subduction process. A similar pattern is also observable in the Caribbean arc. In both the subduction areas we observe also the largest gravity anomalies in the residual maps (Figure 6d), which form a typical dipolar anomaly. Density inhomogeneities due to the trench sediments and the flexural bulge in the oceanic plate are presumably the cause of the dipolar anomaly.

For the African continent we reported the outlines of the Toudeni basin (dark green), which comprises an intercratonic basin, the West African Shield (WAS, orange line) and the Congo Craton. The Toudeni basin and the WAS constitute part of the West African Craton (WAC). The WAC shows generally high values of the slope and error similarly to other shields and Cratons in South America, however a marked negative slope is localized in correspondence of the basin depocenter.

Congo Craton boundaries are well defined by the regression analysis which shows very low values in accordance to the expected high Te values for the area (Pérez-Gussinyé et al., 2009). To the north it is bounded be the Cameroon Volcanic line (CVL), which on contrary shows an almost Airy response, also confirmed by a wavelet analysis of the Bouguer and topography (Pérez-Gussinyé et al., 2009) and by modelling the strength distribution in the lithosphere (Tesauro et al., 2013).

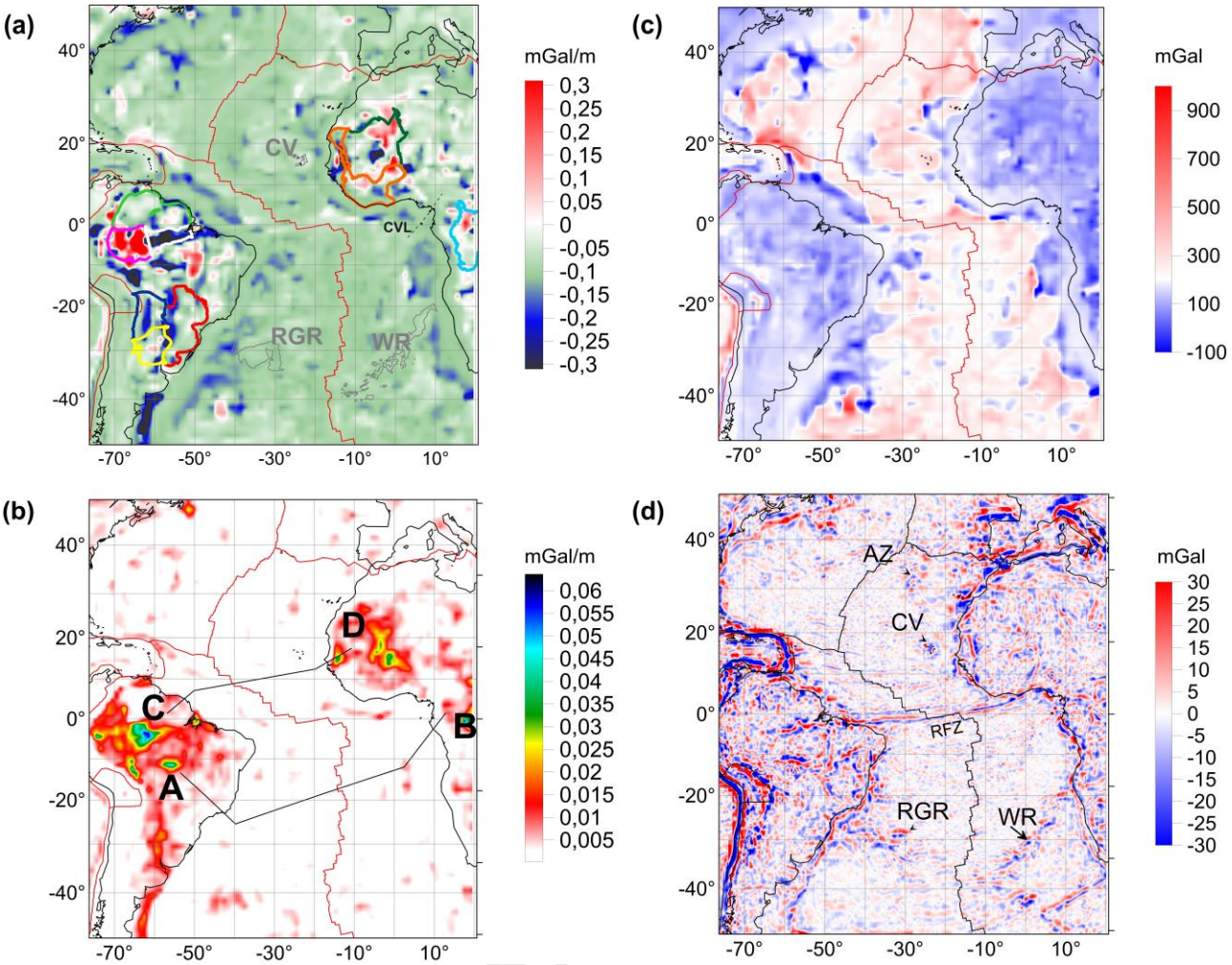

Figure 7. a) Spatial distribution of the slopes regression lines. Outlines of selected geologic units are reported with thick colored lines. Plate boundaries are plotted with the thin red line. Outline of the (Large Igneous Provinces) LIPs for Walvis Ridge (WR), Rio Grande Rise (RGR) and Cape Verde (CV) are reported with gray lines. b) Map of the error on the linear regression coefficient; map reports the traces of the profiles discussed in the text. c) Map of the intercept of the regression line; red line marks the plate boundaries. d) Residuals map; plate boundaries reported with the black line; location of selected LIPs are reported with arrows. The displayed grids are available in the *Research Data* associated to the publication.

In the Atlantic Ocean we observe in general more stable and uniform regression coefficients with respect to continental areas; the values of the slope of the regression line over the oceanic ridge areas are close to the theoretical Bouguer gradient (-0.112 mGal/m). In the synthetic models section we showed that for Pratt isostasy we expect to observe less steep linear coefficients of the regression line over the oceanic areas, with respect to continental orogenic regions such as the Andes, which though is here not observed. An explanation of such behavior could be found in the different topographic wavelengths involved for the ridge and the Andes orogeny. Over the ridge, the main spectral energies of both topography and the Bouguer anomalies are at frequencies lower than 10^{-7} 1/m, while over Andes are in the order of 10^{-6} 1/m (1000 km). The admittance curves in figure 4 show that at spatial frequencies lower than 10^{-7} 1/m for the

Pratt model and lower than 10^{-6} 1/m for Airy the linear regression coefficients tend to the same value, hence not distinguishable.

Regarding the residuals map we observe that oceanic areas show less anomalous values with respect to the continents. The residuals map marks also some important cross-continent tectonic structures, such as the Romanche fracture, which is associated to the Amazonas Rift in South America and seems to penetrate the African continent through the Central African Shear Zone. Similarly, other important magmatic provinces in the Atlantic are emphasized by the residual maps such as the Walvis ridge (WR), Rio Grande Rise (RGR) and the Capo Verde Islands. The Walvis Ridge and Rio Grande Rise show also regression line slopes close to the theoretical value of -0.113 mGal/m implying that the topographic features of the area are nearly in isostatic equilibrium. Recent gravity and seismic analysis conducted by (Constantino et al., 2017) and (Graça et al., 2019) revealing the presence of deep isostatic roots, also confirm this. The Azores, Canary and Cape Verde (CV) islands are on the other hand associated to slightly higher slope values. The discrepancy with respect to WR and RGR could be due to the fact that CV and AZ volcanic islands are nowadays still active and part of the recent volcanic activity is supported by the crustal rigidity.

The Figures 8 and 9 plot two profiles that cross the Atlantic ridge; the locations of the profiles are reported in figure 7b.

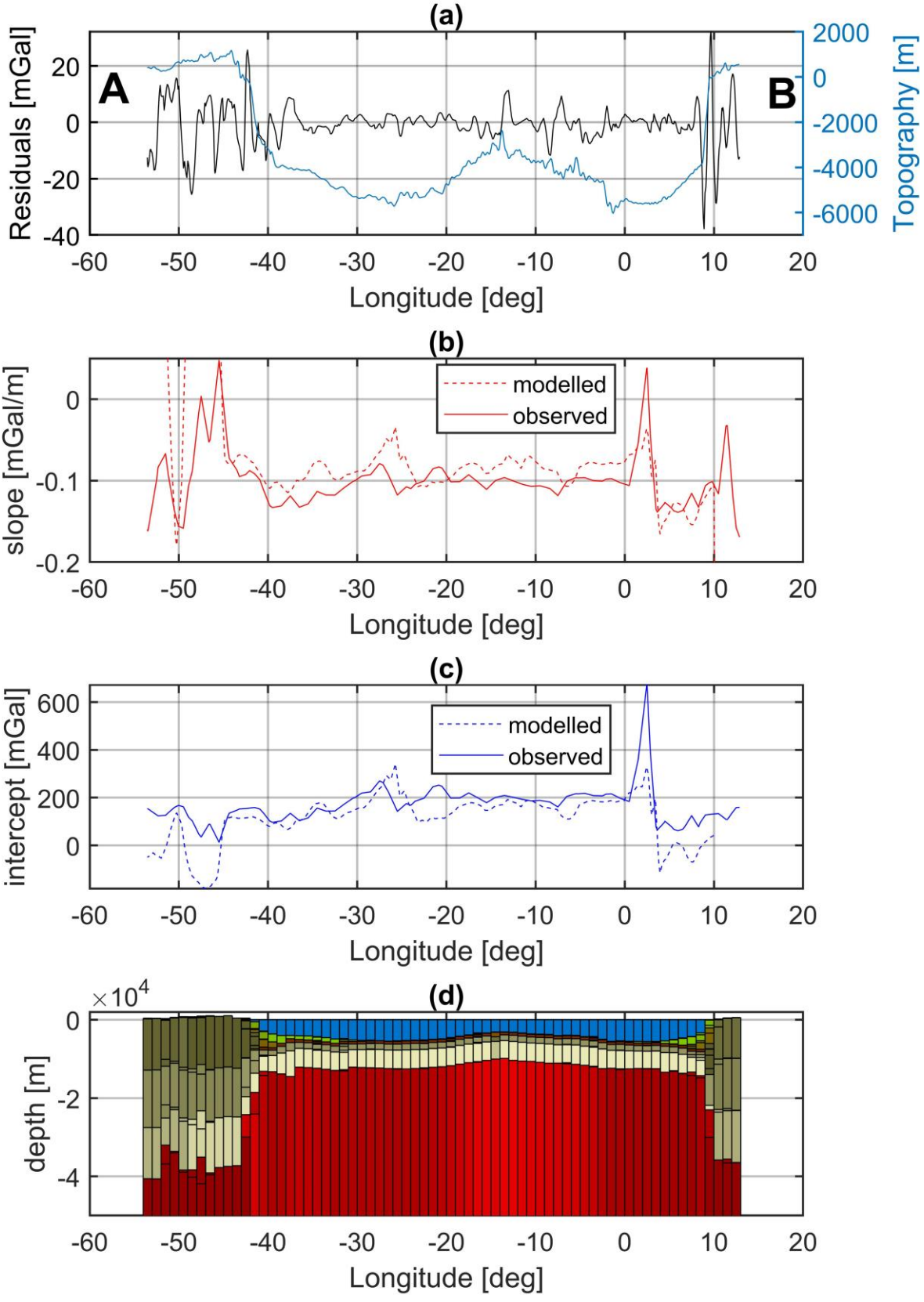
(a)
Residuals [mGal]
Topography [m]
A
B
20
0
-20
-40
2000
0
-2000
-4000
-6000
-60 -50 -40 -30 -20 -10 0 10 20
Longitude [deg]
(b)
slope [mGal/m]
modelled
observed
0
-0.1
-0.2
-60 -50 -40 -30 -20 -10 0 10 20
Longitude [deg]
(c)
intercept [mGal]
modelled
observed
600
400
200
0
-60 -50 -40 -30 -20 -10 0 10 20
Longitude [deg]
(d)
×10^4
depth [m]
0
-2
-4
-60 -50 -40 -30 -20 -10 0 10 20
Longitude [deg]

Figure 8. Profile AB: a) Profile of the topography (blue) and the gravity residuals after the regression analysis (black). b) Slopes of the regression lines along the profiles. Solid line: observed; dashed line: modelled. c) Intercept of the regression lines along the profiles. Solid line: observed; dashed line: modelled. d) Density model along the profile, color code reports the density. Blue: sea with density 1020 kg/m^3; green-dark brown: sediments with densities from 1600 kg/m^3 up to 2600 kg/m^3; ocra to brown: crust from 2600 kg/m^3 to 3000 kg/m^3; red: mantle with densities ranging from 3190 kg/m^{3}up to 3300 kg/m^3.

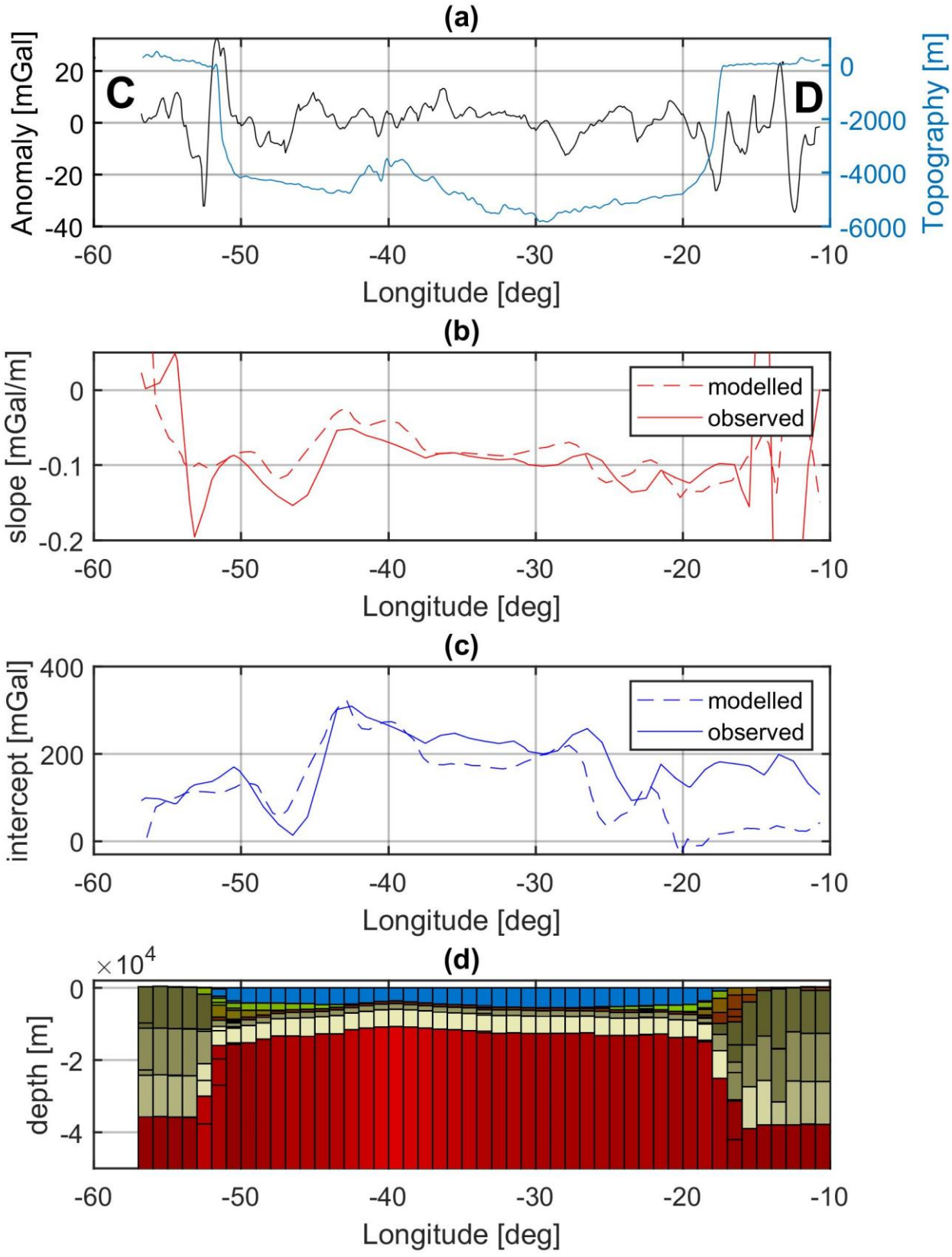
(a)
Anomaly [mGal]
20
0
-20
-40
C
D
0
-2000
-4000
-6000
Topography [m]
-60
-50
-40
-30
-20
-10
Longitude [deg]
(b)
slope [mGal/m]
0
-0.1
-0.2
modelled
observed
Longitude [deg]
(c)
intercept [mGal]
400
200
0
modelled
observed
Longitude [deg]
(d)
×10^4
depth [m]
0
-2
-4
Longitude [deg]

Figure 9. Profile CD: a) Profile of the topography (blue) and the gravity residuals after the regression analysis (black). b) Slopes of the regression lines along the profiles. Solid line: observed; dashed line: modelled. c) Intercept of the regression lines along the profiles. Solid line: observed; dashed line: modelled. d) Density model along the profile, color code reports the density. Blue: sea with density 1020 kg/m^3; green-dark brown: sediments with densities from 1600kg/m^3 up to 2600 kg/m^3; ocra to brown: crust from 2600 kg/m^3 to 3000 kg/m^3; red: mantle with densities ranging from 3190 kg/m^{3}up to 3300 kg/m^3.

In both profiles we observe some common features: the slope (solid red lines in figures 8b and 9b) tends to be almost flat in the central Oceanic regions and over the ridge while it is a bit more negative along the passive margins. Then the slope becomes positive as we approach the outer border of the continent. Intercept (solid blue lines in figures 8c and 9c) mimics the slope in the oceanic domain, while in continent we observe a more complex behavior, as we observe anti-correlation between the two regression coefficients at the beginning of profile AB and a weak positive correlation at the end of profile AB.

Residuals (black lines in figures 8a and 9a) are close to zero over the deepest parts of the oceans, while towards the continental shelf they are characterized by marked positive-negative dipolar anomalies.

In order to quantitatively interpret the regression coefficients we perform the regression analysis over a realistic synthetic lithosphere model of the Central Atlantic region. The simulated gravity fields are constrained by the crustal structure and densities derived from the CRUST1.0 model (Laske et al., 2013). We also included the lithospheric mantle assuming a unique density for the continental areas (3280 kg/m^3), and a laterally varying density for the oceanic areas. The mantle densities for oceans were calculated assuming Pratt mechanism with compensation depth set to 120 km, similarly to the approach proposed by (Szwillus et al., 2016). The gravity effects of a reference lithosphere model were then subtracted from the simulated gravity fields in order to obtain the Free-air gravity anomaly map. The Bouguer field is then obtained by removing the topo-bathymetric effects, calculated using a unique crustal density value, from the Free-air anomalies.

The regression analysis was then performed with the same window parameters as the real case, with a window analysis of 3°x3°. We report the results over the same profiles shown in figure 8.

The density model is shown in figures 9c and 10c with a color code according to the different layers of CRUST1.0 model: red for lithospheric mantle, ocra for crust, green/brown for sediments and blue for sea water. The variations of the color intensity of each layer represent variations in the density of each layer.

The simulated regression parameters along the profiles are plotted in figures 8b-c and 9b-c with dashed lines; in both the profiles a good correspondence between the modelled and observed values is found. We see that the minima in the slope profiles are located in proximity of the continent boundary where a huge sediment accumulation at the passive margin occurs.

Approaching the continents, the linear regression coefficients show larger variations justified by the presence of the rigid shields and cratons in both South America and Africa margins. Over these areas, the correspondence between modelled and observed values is also worse, as effect of the uncertainties in the CRUST1.0 model.

The intercept profiles show systematically positive values over the oceanic plains, tending to zero as we approach the continental margins. This behavior is in accordance to what we have presented in the synthetic models section.

4 Application on the gravity field of Mars

We apply the regression analysis on the topography and gravity field of Mars, to identify main characteristics and use them to discriminate lateral density variations and differences in the isostatic support of the topography. The spherical harmonic model of gravity is ggm1025a, an update of the GMM-2B model of (Lemoine et al., 2001), available on the ICGEM calculation service up to degree and order 80. The spherical harmonic expansion of topography is derived from the MOLA (Mars Orbiter Laser Altimeter) mission and is available from the NASA PDS Geosciences Node (https://pds-geosciences.wustl.edu/).

The gravity disturbance is calculated at a height of 50 km above the reference ellipsoid. The Bouguer gravity disturbance is obtained by discretizing the topography with tesseroids (Uieda et al., 2016), assigning a crustal density of 2950 kg/m^3 (Steinberger et al., 2010). Tesseroids are spherical prisms and preferable to rectangular prisms for a global calculation of gravity effect. The Mars ellipsoid was defined with the parameters of major axis =3398627 m, and flattening f=1/169.8 (Smith et al., 1999). In figure 10 the fields and topography are mapped.

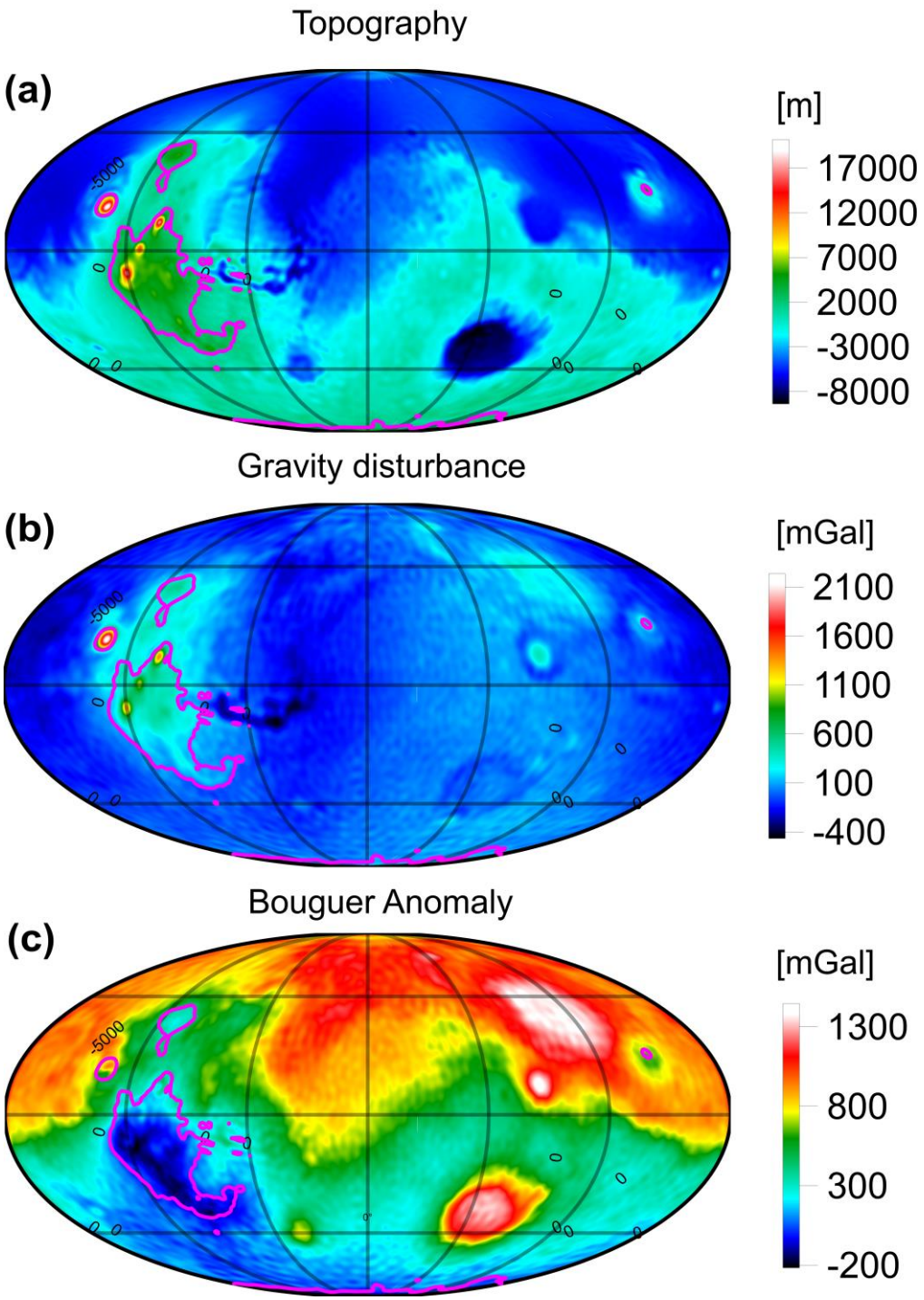

Figure 10. Global models of topography and gravity for Mars. a) Topography. b) Gravity disturbance calculated at 50 km height. c) Bouguer anomaly map. In all figures purple outline marks the highest landmarks and the Tharsis province.

The equatorial region for longitudes between 220° E and 300° E (purple line), named the Tharsis province, is known to be volcanic and is recognized by the highest landmarks, reaching up to 20 km height. The lithospheric flexural analysis identifies this area with increased *Te* values close to 150 km (Zuber, 2000). The regression analysis on windows of 7° by 7° results in characteristic values of slope and intercept (Figure 11),

with median value of slope and intercept equal to -0.06 mGal/m and 322 mGal, and root mean square values from the mean of 0.136 mGal/m and 774.3 mGal, respectively. Similar values are obtained for larger window size (see Table 1), showing that the analysis is robust against choice of window. The regression is well defined, with small errors of regression parameters (e.g. slope errors less than 15 % of slope value) over a large area of Mars, except for the northern polar region. A less negative slope, an indication of increased crustal density and/or reduction in crustal thickness compensation, characterizes the Tharsis province. The Hellas impact basin (black outline; longitude 70° East, latitude 45° South) has a double couple slope and intercept in its innermost part, distinguishing a marginal ring from the internal basin. A profile across the Tharsis province illustrates the increase of slope over the tall topographic reliefs. The Bouguer slightly anticorrelates with the long wavelength of the topography, but not with the short wavelength. Infact, Bouguer positively correlates with the short wavelength topography, an indication of increased crustal density or reduced crustal thickening. This feature is well represented in the less negative slopes and increase of intercept. The slope and intercept have greater variability in the Northern Lowlands (Smrekar et al., 2018), whereas in the Southern Highlands the slope is mostly coherently negative and the intercept is more uniform limited to about 400 mGal.

Window size	**Median slope/Standard deviation from mean**	**Median intercept/standard deviation from mean**
7° x 7°	-0.06 mGal/m 0.136 mGal/m	322 mGal 774.3 mGal
13° x 13°	-0.069 mGal/m 0.114 mGal/m	317 mGal 607 mGal

Table 1. Statistical values of regression parameters for Mars.

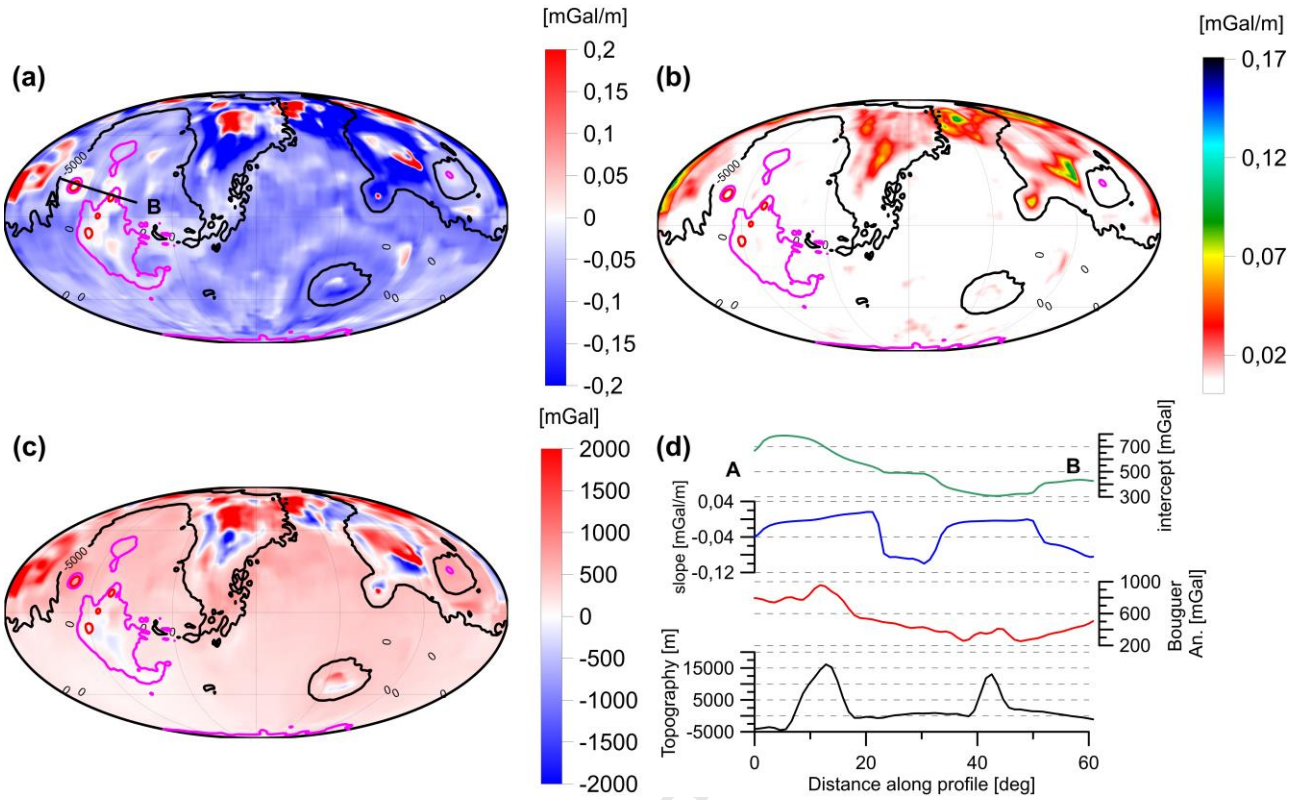

Figure 11. Spatial distribution of the regression parameters over the Mars planet. a) Slope of the regression line b) Error on the slope coefficient. c) Intercept of the regression line d) Profile of the regression coefficients along the Tharsis region. Trace of the profile reported in Figure 11a. The displayed grids are available in the *Research Data* associated to the publication.

5 Slope and intercept spatial distribution

We have seen in section 3 that the Earth's Oceanic areas seem to be associated typically with high values of intercept and stable linear regression coefficients; continental margins are characterized, on the other hand, by lower values of intercepts and steeper regression lines. From these considerations emerges the possibility to map the main geologic and geodynamic structures of Earth, and also of Mars, according to the joint distribution of the regression coefficients.

The relation between slopes and intercept seems to be deterministic as can be seen by the grey dots in the scatterplot of Figure 12a,c. The displayed datapoints are limited to well defined slopes, in the sense that the ratio between error and absolute slope value is smaller than 1/50. This threshold limits the values greatly to offshore areas and the Andes (green dots in Figure 12b). The data points are distributed in several clusters of slope and intercept.

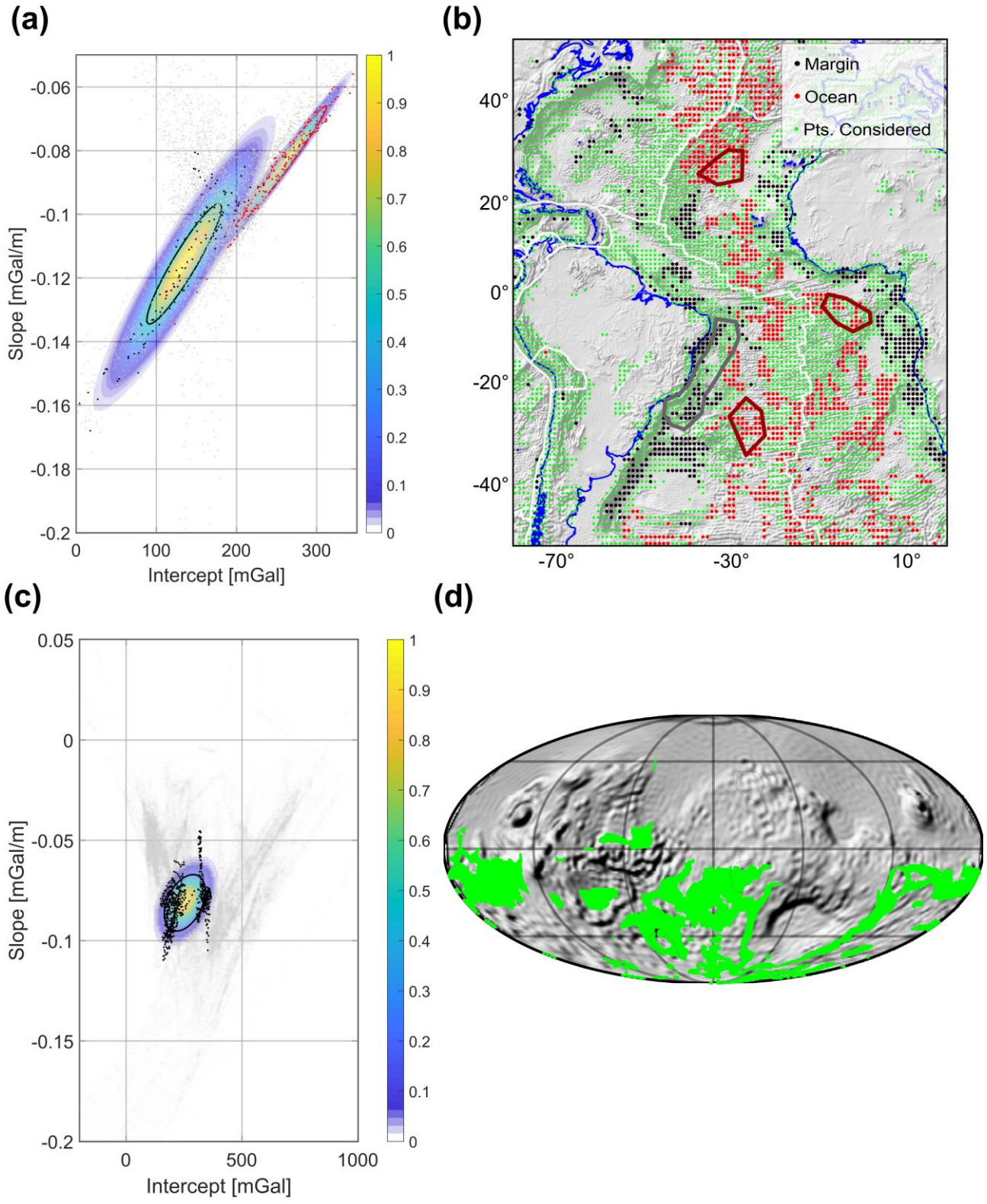

Figure 12. Maximum likelihood classification of oceanic and marginal crust through slope and intercept in the Atlantic basin and on Mars. a) Scatter plot of slope and intercept values of the regression analysis (grey dots). Red dots: undisturbed oceanic crust; black dots: continental margin. Color code: Gaussian maximum likelihood classifier; red line: equiprobability contour of 0.2 for undisturbed oceanic crust; black line equiprobability contour of 0.5. b) Classified pixels according to: undisturbed oceanic areas (red dots), continental margin areas (grey dots); areas with low slope error (green dots). Training area for undisturbed oceanic crust: dark red outline; for continental margin: gray outline. c) Scatter plot of slope and intercept values of the regression

analysis (grey dots). Black dots: undisturbed Martian crust. Color code: Gaussian maximum likelihood classifier; black line equiprobability contour of 0.2. d) Classified pixels according to: undisturbed Martian crust (green dots). Training area for undisturbed Martian crust: black outlines.

With the aim of using the slope and intercept distribution for a Maximum Likelihood classification of the oceanic areas, we define a "training area" of undisturbed oceanic crust, and map these pixels on the slope/intercept graph. With the term undisturbed oceanic crust, we define the oceanic lithosphere without sedimentary basins or other superposed geologic structures. The red outlines in Figure 12b show the training areas of oceanic crust from the central Atlantic ridge, the red dots in Figure 12a their collocation in the slope/intercept graph. We calculate the average value and covariance matrix of these values (Table 2), from which the bivariate Gaussian distribution is defined (Lillesand et al., 2015).

Earth Ocean			**Earth Margin**			**Mars**		
	Int	**Slo**		**Int**	**Slo**		**Int**	**Slo**
Int	1712.70	0.574	**Int**	3124.87	1.182	**Int**	31588.08	1.362
Slo	0.574	1.98E-04	**Slo**	1.182	5.17E-04	**Slo**	1.362	0.0002

Table 2. Covariance matrices between the two regression parameters slope (Slo) and intercept (Int) for the two clusters on the Earth and for Martian undisturbed crust.

The Gaussian function defines the maximum likelihood classifier for the class of oceanic crust, the equiprobability is mapped with color codes in Figure 12a. The red contour shows the 0.2 equiprobablity contour. All red dots in Figure 12b are the pixels that the classifier maps as belonging to the class of oceanic crust. We define a second class, which is continental margin, with the outline of the training area in black in Figure 12b. The Gaussian maximum likelihood classifier is again calculated and mapped in Figure 12a, and the 0.5 equiprobablity contour shown in black. Given the larger dispersion of the distribution, we have chosen a higher probability threshold. The grey dots in Figure 12b are those, which are classified as belonging to the class margin by the maximum likelihood classifier. The areas belonging to the same class, can be considered to have similar density structure of the crust. The overall reduction of slope, which is found along the continental margin is presumably due to the sediment deposits on top of the oceanic crust, which distinguishes the reduction of bathymetric depths towards the continent from those toward the central ridge through the underlying density. An in depth analysis of the different classes is beyond the scope of the present work.

We have tested the classification through the cluster analysis also directly on the Bouguer and topography values. Exploiting the same classification algorithm over the training areas defined in figure 12b to the Bouguer and topographic data we perform a new classification of the ocean and margin areas. The results are shown in the Appendix and generally are consistent with the results obtained using slope and intercept.

However the classification based on slope and intercept of the regression lines performs better in the continental margins (see Appendix for further comments).

We extend the cluster analysis of slope and intercept also to Mars (Figure 12c and Figure 12d). We define one class as standard Mars structure, which has the most common occurrence of slope and intercept values. The class has two definitions, either through a training area over a region with homogenous regression values, or by analyzing the statistical distribution of the slope and intercept values. We have tested both approaches, which define a very similar class, which we could define as undisturbed Martian crustal structure. The training areas, maximum likelihood distribution, and identified class pixels are shown in Figure 12 c,d, analogously to the definitions made for the Atlantic ocean.

6 Discussion

The regression analysis proved to be a useful tool to study the lithosphere structure and to separate the different sources that contribute to the observed Bouguer signal. The analysis could be performed over sliding windows in order to capture variations in the mechanical response to topographic loads of the lithosphere. The obtained residual map can be regarded as an isostatic anomaly map in which the anomalies are due to unaccounted density variations with respect to a crust with homogeneous density.

The regression coefficients maps, in particular the slope of the regression line, contain important information about the isostatic state of the investigated area and are able to differentiate large-scale geological structures. In the Central Atlantic area and in the surrounding African and South American regions we obtained a map of the linear regression coefficient that is largely correlated to the elastic thickness of the lithosphere. Areas with low *Te* values are associated to stable regression coefficients with slope values close to the theoretical simple Bouguer gradient $-2\,\pi\,G\,\rho c$ with ρc the density used for terrain correction; rigid crusts and lithospheres are usually characterized by less steep linear regression coefficients. Over continents and continental shelfs, where the density structure is more heterogeneous, the linear coefficient is able to mark different geological provinces, such as sedimentary basins, shields and cratons. In the Central Atlantic region significant variations of the slope are observed in a narrow strip area that bounds the shelf; here we observe a steeper slope of the regression line with respect to offshore oceanic areas. Our synthetic model reveals a correlation of these slopes minima with the sedimentary structures of the shelf. The Continental Ocean Boundary (COB) is likely to be located inside the area comprised by the coastline and these slopes minima.

For Mars we observed that the regression analysis is able to discriminate, similarly to the earth case, the most prominent geologic structures as the Tharsis region or the Hellas impact basin.

The residual maps contain the gravity signals not directly correlated to topography and consequently could be related to density inhomogeneities not accounted in the isostatic model (geologic effect). If one is interested in inverting the residuals in terms of causative bodies, the analyst should pay attention that the window area selected for the analysis should be large enough to detect the isostatic signal. Small windows could partly erode the geologic signal of interest from the residual maps; this could be the case of large sedimentary basins for instance such as Amazon and Congo basins. Enlarging the windows dimension for the analysis or using predetermined regression coefficients calculated over similar geodynamic settings could be an approach to overcome this problem.

The analysis of relationship between gravity and topography analysis is classically done in geodesy calculating admittance or coherency attributes (for an extensive review see (Kirby, 2014)) and fitting a flexural model; then a map of the spatial variations of the *Te* is obtained. With respect to these approaches, the regression method could hardly offer quantitative estimates of the elastic properties of the crust, mainly because the linear regression coefficient is biased by its sensitivity also to crustal heterogeneities.

We have shown the potential of the joint analysis of the intercept and slopes: in our application we derived typical regression coefficient pairs from selected small areas and then use these values to map the whole study area. We believe this cluster analysis and the relative classification represents an important and fast method for globally mapping the principal crustal features, applicable both to Earth or to other celestial bodies.

6 Conclusion

Given its simplicity and its fast implementation the regression method seems to offer a powerful tool for a quick analysis of global gravity fields and a preliminary interpretation of the large scale structures of the earth and other celestial bodies. The method belongs to the Machine learning techniques and the regression parameters can be integrated with other observed variables, such as heat flow, magnetic susceptibility maps and seismic wave velocity. We have demonstrated the potential of the regression parameters to distinguish terrains on Earth and Mars, and the analysis can analogously be expanded to other planets and celestial bodies. For the Earth Atlantic Oceanic crust, the regression parameters cluster in such a way to distinguish the central Atlantic oceanic crust from the continental passive margins. This analysis can be analogously extended to other oceanic basins and other tectonic domains, investigating the specific cases of subduction, fracture zones, and volcanic oceanic domains.

Acknowledgements

Funding of Tommaso Pivetta by the EUSALP Project is thankfully acknowledged.

References

Assumpção, M., Feng, M., Tassara, A., Julià, J., 2013. Models of crustal thickness for South America from seismic refraction, receiver functions and surface wave tomography. Tectonophysics 609, 82–96. https://doi.org/10.1016/j.tecto.2012.11.014

Braitenberg, C., 2015. Exploration of tectonic structures with GOCE in Africa and across-continents. International Journal of Applied Earth Observation and Geoinformation 35, 88–95. https://doi.org/10.1016/j.jag.2014.01.013

Braitenberg, C., Ebbing, J., 2009. The GRACE-satellite gravity and geoid fields in analysing large-scale, cratonic or intracratonic basins. Geophysical Prospecting 57, 559–571. https://doi.org/10.1111/j.1365-2478.2009.00793.x

Braitenberg, C., Mariani, P., De Min, A., 2013. The European Alps and Nearby Orogenic Belts Sensed by GOCE. Boll. Geofis. Teor. Appl. 54, 321–334. https://doi.org/10.4430/bgta0105

Bucha, B., Janák, J., 2013. A MATLAB-based graphical user interface program for computing functionals of the geopotential up to ultra-high degrees and orders. Computers & Geosciences 56, 186–196. https://doi.org/10.1016/j.cageo.2013.03.012

Caratori Tontini, F., Graziano, F., Cocchi, L., Carmisciano, C., Stefanelli, P., 2007. Determining the optimal Bouguer density for a gravity data set: implications for the isostatic setting of the Mediterranean Sea. Geophysical Journal International 169, 380–388. https://doi.org/10.1111/j.1365-246X.2007.03340.x

Chappell, A.R., Kusznir, N.J., 2008. Three-dimensional gravity inversion for Moho depth at rifted continental margins incorporating a lithosphere thermal gravity anomaly correction. Geophysical Journal International 174, 1–13. https://doi.org/10.1111/j.1365-246X.2008.03803.x

Coffin, M.F., Gahagan, L.M., Lawver, L.A., 1998. Present-day Plate Boundary Digital Data Compilation. University of Texas Institute for Geophysics Technical Report 174, 1–5.

Constantino, R.R., Hackspacher, P.C., de Souza, I.A., Lima Costa, I.S., 2017. Basement structures over Rio Grande Rise from gravity inversion. Journal of South American Earth Sciences 75, 85–91. https://doi.org/10.1016/j.jsames.2017.02.005

Ebbing, J., Haas, P., Ferraccioli, F., Pappa, F., Szwillus, W., Bouman, J., 2018. Earth tectonics as seen by GOCE - Enhanced satellite gravity gradient imaging. Scientific Reports 8. https://doi.org/10.1038/s41598-018-34733-9

Förste, C., Bruinsma, S., Rudenko, S., Abrikosov, O., Lemoine, J.-M., Marty, J.-C., Neumayer, K.H., Biancale, R., 2016. EIGEN-6S4 A time-variable satellite-only gravity field model to d/o 300 based on LAGEOS, GRACE and GOCE data from the collaboration of GFZ Potsdam and GRGS Toulouse. https://doi.org/10.5880/icgem.2016.004

Genova, A., Goossens, S., Lemoine, F.G., Mazarico, E., Neumann, G.A., Smith, D.E., Zuber, M.T., 2016. Seasonal and static gravity field of Mars from MGS, Mars Odyssey and MRO radio science. Icarus 272, 228–245. https://doi.org/10.1016/j.icarus.2016.02.050

Graça, M.C., Kusznir, N., Gomes Stanton, N.S., 2019. Crustal thickness mapping of the central South Atlantic and the geodynamic development of the Rio Grande Rise and Walvis Ridge. Marine and Petroleum Geology 101, 230–242. https://doi.org/10.1016/j.marpetgeo.2018.12.011

Hirt, C., Reußner, E., Rexer, M., Kuhn, M., 2016. Topographic gravity modeling for global Bouguer maps to degree 2160: Validation of spectral and spatial domain forward modeling

techniques at the 10 microGal level: TOPOGRAPHIC GRAVITY MODELING. Journal of Geophysical Research: Solid Earth 121, 6846–6862. https://doi.org/10.1002/2016JB013249

Kirby, J.F., 2014. Estimation of the effective elastic thickness of the lithosphere using inverse spectral methods: The state of the art. Tectonophysics 631, 87–116. https://doi.org/10.1016/j.tecto.2014.04.021

Laske, G., Masters, G., Ma, Z., Pasyanos, M., 2013. Update on CRUST1.0 - A 1-degree Global Model of Earth's Crust. Presented at the EGU General Assembly 2013, 7-12 April, 2013, Vienna, Austria.

Lemoine, F.G., Smith, D.E., Rowlands, D.D., Zuber, M.T., Neumann, G.A., Chinn, D.S., Pavlis, D.E., 2001. An improved solution of the gravity field of Mars (GMM-2B) from Mars Global Surveyor. Journal of Geophysical Research: Planets 106, 23359–23376. https://doi.org/10.1029/2000JE001426

Lillesand, T.M., Kiefer, R.W., Chipman, J.W., 2015. Remote sensing and image interpretation, Seventh edition. ed. John Wiley & Sons, Inc, Hoboken, N.J.

Mariani, P., Braitenberg, C., Ussami, N., 2013. Explaining the thick crust in Paraná basin, Brazil, with satellite GOCE gravity observations. Journal of South American Earth Sciences 45, 209–223. https://doi.org/10.1016/j.jsames.2013.03.008

Nettleton, L.L., 1939. DETERMINATION OF DENSITY FOR REDUCTION OF GRAVIMETER OBSERVATIONS*. GEOPHYSICS 4, 176–183. https://doi.org/10.1190/1.0403176

Pastorutti, A., Braitenberg, C., 2019. A geothermal application for GOCE satellite gravity data: modelling the crustal heat production and lithospheric temperature field in Central Europe. Geophysical Journal International 219, 1008–1031. https://doi.org/10.1093/gji/ggz344

Pérez-Gussinyé, M., Metois, M., Fernández, M., Vergés, J., Fullea, J., Lowry, A.R., 2009. Effective elastic thickness of Africa and its relationship to other proxies for lithospheric structure and surface tectonics. Earth and Planetary Science Letters 287, 152–167. https://doi.org/10.1016/j.epsl.2009.08.004

Persits, F., Ahlbrandt, T., Tuttle, M., Charpentier, R., Brownfield, M., Takahashi, K., 1997. Map showing geology, oil and gas fields, and geological provinces of Africa. USGS Open-File Report 97-470A.

Rexer, M., Hirt, C., Claessens, S., Tenzer, R., 2016. Layer-Based Modelling of the Earth's Gravitational Potential up to 10-km Scale in Spherical Harmonics in Spherical and Ellipsoidal Approximation. Surveys in Geophysics 37, 1035–1074. https://doi.org/10.1007/s10712-016-9382-2

Schenk, C.J., Viger, R.J., Anderson, C.P., 1997. Maps showing geology, oil and gas fields and geologic provinces of the South America region. USGS Open-File Report 97-470D.

Smith, D.E., Zuber, M.T., Solomon, S.C., Phillips, R.J., Head, J.W., Garvin, J.B., Banerdt, W.B., Muhleman, D.O., Pettengill, G.H., Neumann, G.A., Lemoine, F.G., Abshire, J.B., Aharonson, O., David, C., Brown, Hauck, S.A., Ivanov, A.B., McGovern, P.J., Zwally, H.J., Duxbury, T.C., 1999. The Global Topography of Mars and Implications for Surface Evolution. Science 284, 1495–1503. https://doi.org/10.1126/science.284.5419.1495

Smrekar, S.E., Lognonné, P., Spohn, T., Banerdt, W.B., Breuer, D., Christensen, U., Dehant, V., Drilleau, M., Folkner, W., Fuji, N., Garcia, R.F., Giardini, D., Golombek, M., Grott, M., Gudkova, T., Johnson, C., Khan, A., Langlais, B., Mittelholz, A., Mocquet, A., Myhill, R., Panning, M., Perrin, C., Pike, T., Plesa, A.-C., Rivoldini, A., Samuel, H., Stähler, S.C., van Driel, M., Van Hoolst, T., Verhoeven, O., Weber, R., Wieczorek, M., 2018. Pre-mission InSights on the Interior of Mars. Space Sci Rev 215, 3. https://doi.org/10.1007/s11214-018-0563-9

Steinberger, B., Werner, S.C., Torsvik, T.H., 2010. Deep versus shallow origin of gravity anomalies, topography and volcanism on Earth, Venus and Mars. Icarus 207, 564–577. https://doi.org/10.1016/j.icarus.2009.12.025

Szwillus, W., Ebbing, J., Holzrichter, N., 2016. Importance of far-field topographic and isostatic corrections for regional density modelling. Geophys J Int 207, 274–287. https://doi.org/10.1093/gji/ggw270

Tassara, A., Swain, C., Hackney, R., Kirby, J., 2007. Elastic thickness structure of South America estimated using wavelets and satellite-derived gravity data. Earth and Planetary Science Letters 253, 17–36. https://doi.org/10.1016/j.epsl.2006.10.008

Tesauro, M., Kaban, M.K., Cloetingh, S.A.P.L., 2013. Global model for the lithospheric strength and effective elastic thickness. Tectonophysics 602, 78–86. https://doi.org/10.1016/j.tecto.2013.01.006

Uieda, L., Barbosa, V.C.F., Braitenberg, C., 2016. Tesseroids: Forward-modeling gravitational fields in spherical coordinates. GEOPHYSICS 81, F41–F48. https://doi.org/10.1190/geo2015-0204.1

Watts, A.B., 2001. Isostasy and flexure of the lithosphere. Cambridge University Press, Cambridge ; New York.

Wirnsberger, H., Krauss, S., Mayer-Gürr, T., 2019. First independent Graz Lunar Gravity Model derived from GRAIL. Icarus 317, 324–336. https://doi.org/10.1016/j.icarus.2018.08.011

Zampa, L.S., Tenzer, R., Eshagh, M., Pitoňák, M., 2018. Evidence of mantle upwelling/downwelling and localized subduction on Venus from the body-force vector analysis. Planetary and Space Science 157, 48–62. https://doi.org/10.1016/j.pss.2018.03.013

Zhao, G., Chen, B., Uieda, L., Liu, J., Kaban, M.K., Chen, L., Guo, R., 2019. Efficient 3-D Large-Scale Forward Modeling and Inversion of Gravitational Fields in Spherical Coordinates With Application to Lunar Mascons. Journal of Geophysical Research: Solid Earth. https://doi.org/10.1029/2019JB017691

Zuber, M.T., 2000. Internal Structure and Early Thermal Evolution of Mars from Mars Global Surveyor Topography and Gravity. Science 287, 1788–1793. https://doi.org/10.1126/science.287.5459.1788

Appendix

We applied the cluster analysis algorithm presented in section 5 to the Bouguer and the filtered topography in order to compare the performance with the slope and intercept classification. We used the same training areas as reported in figure 12b.

Figure A1 shows the scatter plot of the topo/bathymetry and Bouguer together with the Gaussian maximum probability classifier reported with the color code. The black line reports the equiprobability contour of 0.5 for the continental margin areas while the red line shows the equiprobability contour of 0.2 for the oceanic areas.

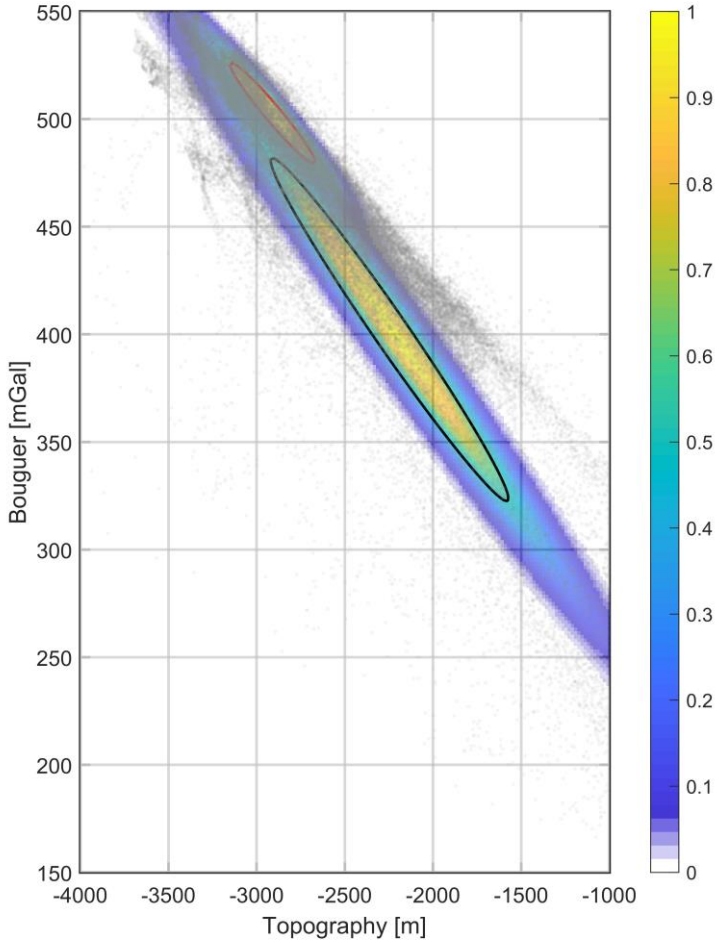

A1. Maximum likelihood classification of oceanic and marginal crust through Bouguer and bathymetry in the Atlantic basin. Scatter plot of bathymetry and Bouguer values (grey dots). Color code: Gaussian maximum likelihood classifier; red line: equiprobability contour of 0.2 for oceanic crust; black line equiprobability contour of 0.5.

The following figure A2 reports the classified regions according to the oceanic and passive continental margin areas (respectively red and black dots). Comparing figure A2 with figure 12b we observe a good consistency in both the classified areas. The classification with the regression parameters appears to perform better over the passive continental margin, limiting the erroneous classification of the ridge at about -50°E, 20°N and excluding the active margin along the Andes.

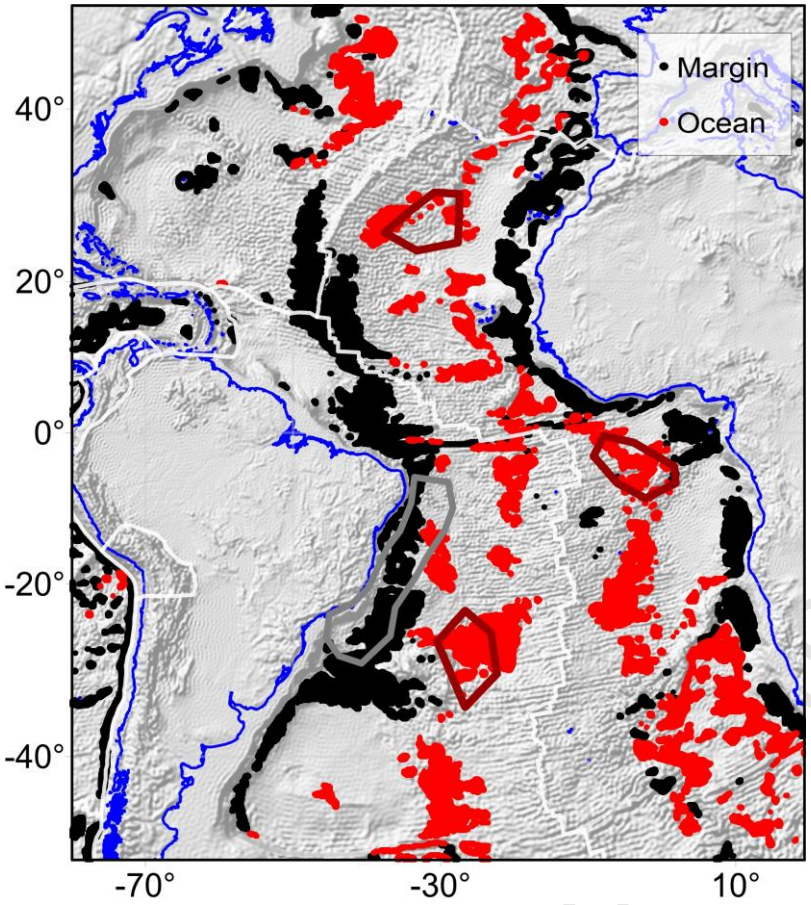

A2. Classified pixels of oceanic (red dots) and continental passive margin areas (black dots) through Bouguer and bathymetry in the Atlantic. Training area for undisturbed oceanic crust: dark red outline; for continental margin: gray outline.

Declaration of interests

☒ The authors declare that they have no known competing financial interests or personal relationships that could have appeared to influence the work reported in this paper.

☐The authors declare the following financial interests/personal relationships which may be considered as potential competing interests:

Highlights

- **Easily accessible global Gravity field require non-specialist interpretation methods**
- **Regression parameters of gravity and topography reflect crust and lithosphere structure**
- **Regression has dual purpose of gravity residualization and identification of tectonic domains differentiated by sediment cover, age and magmatic emplacement.**
- **Regression is related to isostasy but bears surplus information, due to the intercept term which is not considered in flexure analysis**
- **The gravity and topography is illustrated to classify Earth and Mars terranes**

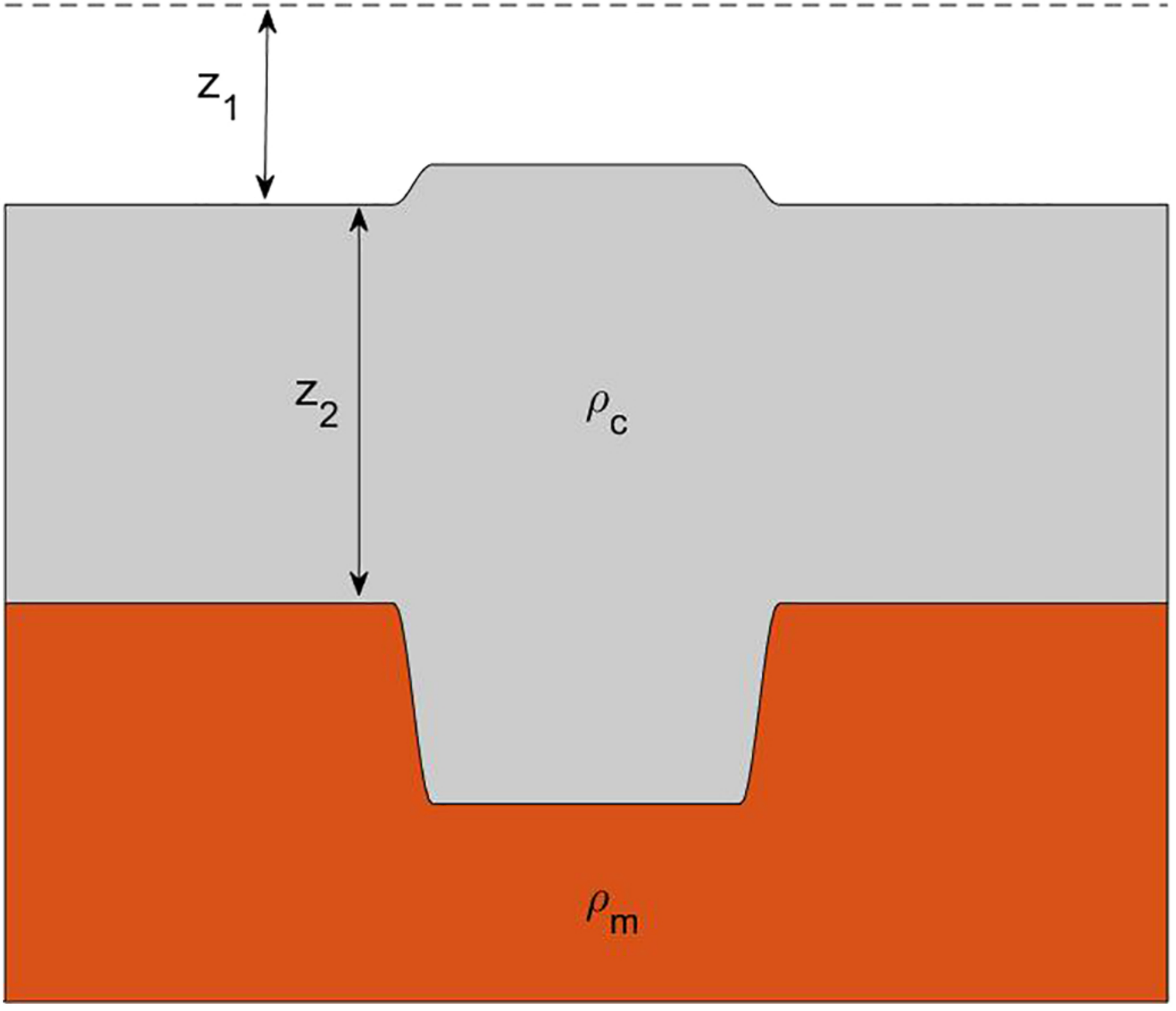

Figure 1

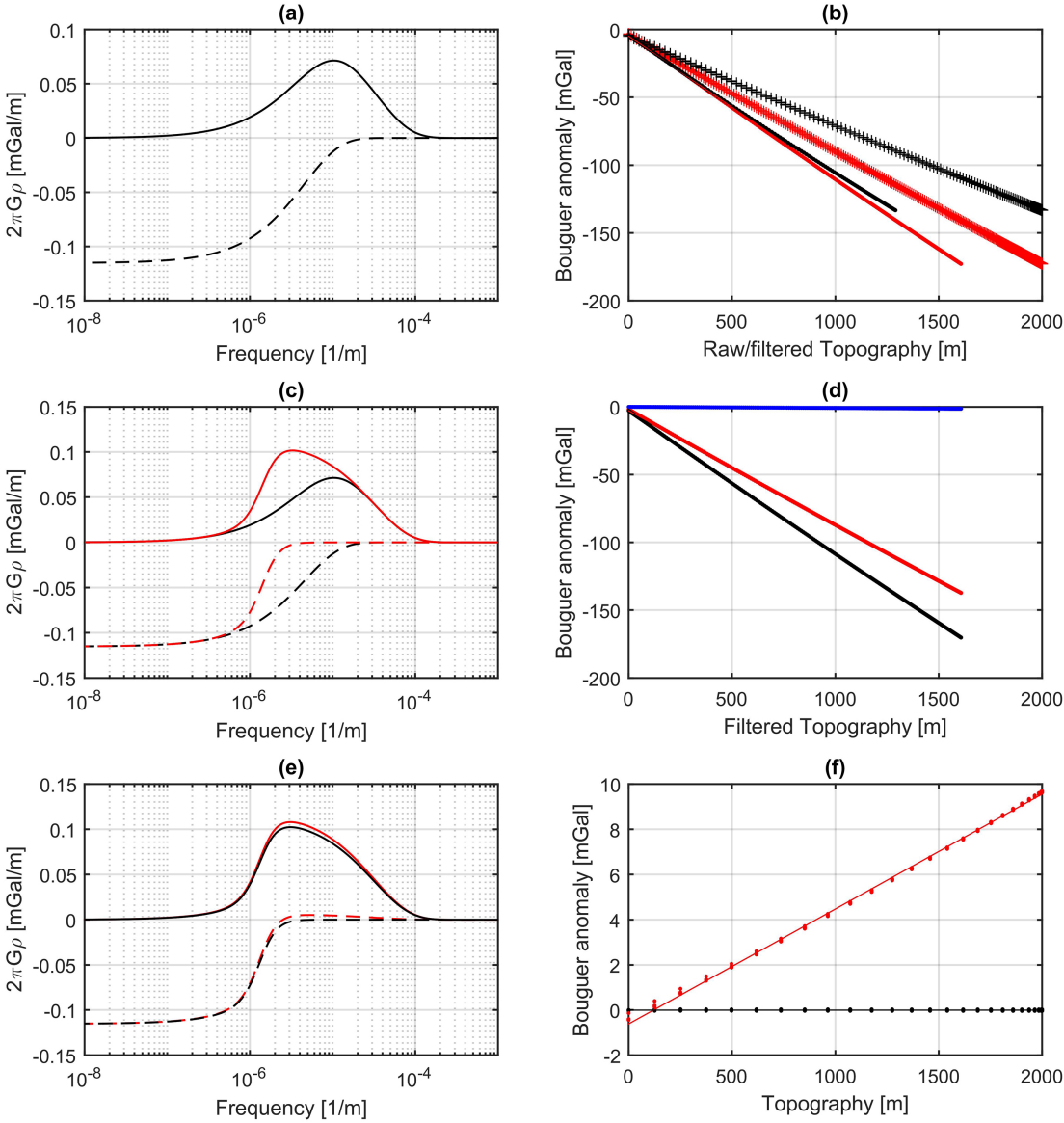
(a)
0.1
0.05
0
-0.05
-0.1
-0.15
$2\pi G\rho$ [mGal/m]
10^{-8}
10^{-6}
10^{-4}
Frequency [1/m]
(b)
0
-50
-100
-150
-200
Bouguer anomaly [mGal]
0
500
1000
1500
2000
Raw/filtered Topography [m]
(c)
0.15
0.1
0.05
0
-0.05
-0.1
-0.15
$2\pi G\rho$ [mGal/m]
10^{-8}
10^{-6}
10^{-4}
Frequency [1/m]
(d)
0
-50
-100
-150
-200
Bouguer anomaly [mGal]
0
500
1000
1500
2000
Filtered Topography [m]
(e)
0.15
0.1
0.05
0
-0.05
-0.1
-0.15
$2\pi G\rho$ [mGal/m]
10^{-8}
10^{-6}
10^{-4}
Frequency [1/m]
(f)
10
8
6
4
2
0
-2
Bouguer anomaly [mGal]
0
500
1000
1500
2000
Topography [m]

Figure 2

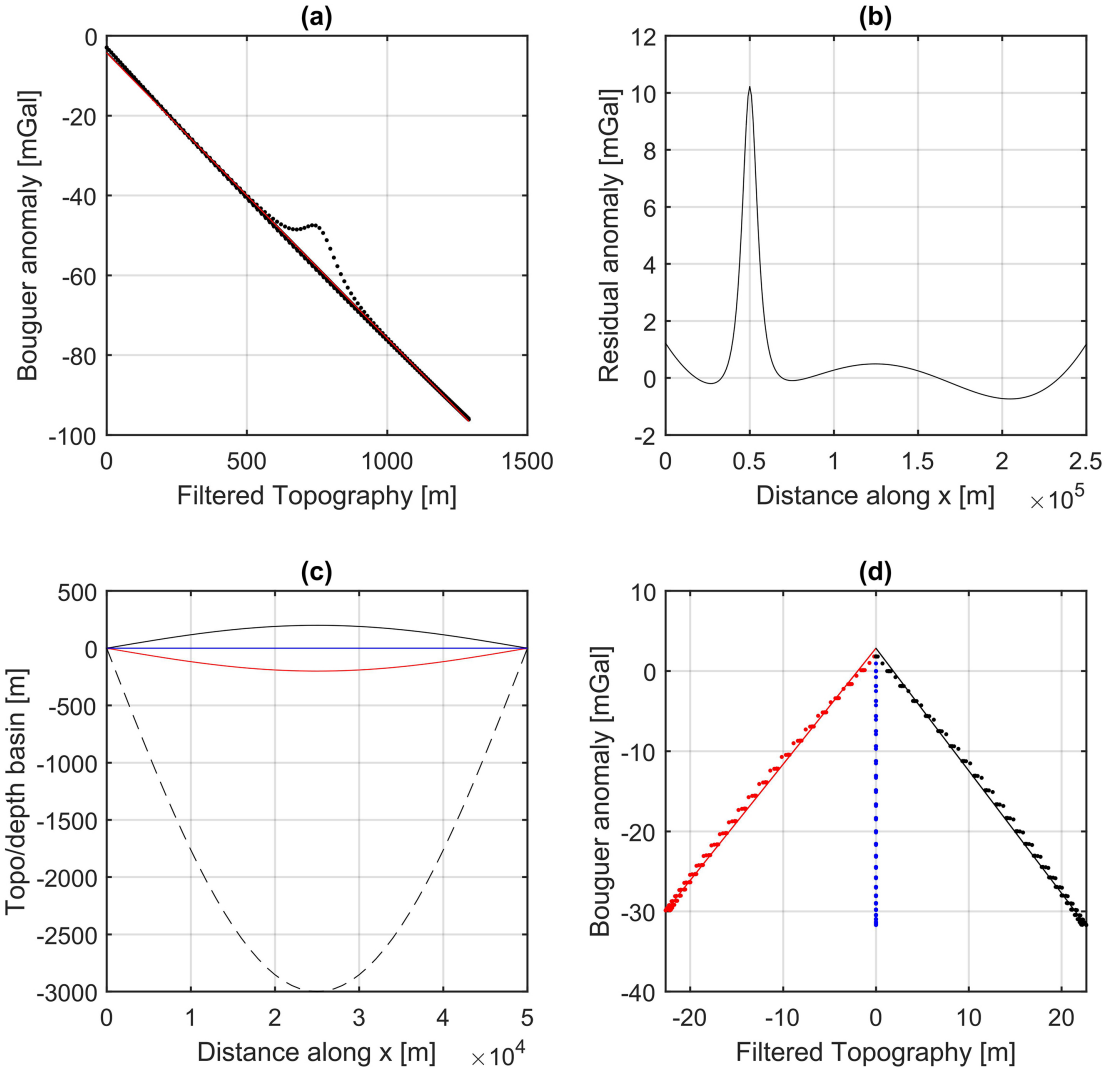
(a)
Bouguer anomaly [mGal]
Filtered Topography [m]
(b)
Residual anomaly [mGal]
Distance along x [m]
×10^5
(c)
Topo/depth basin [m]
Distance along x [m]
×10^4
(d)
Bouguer anomaly [mGal]
Filtered Topography [m]

Figure 3

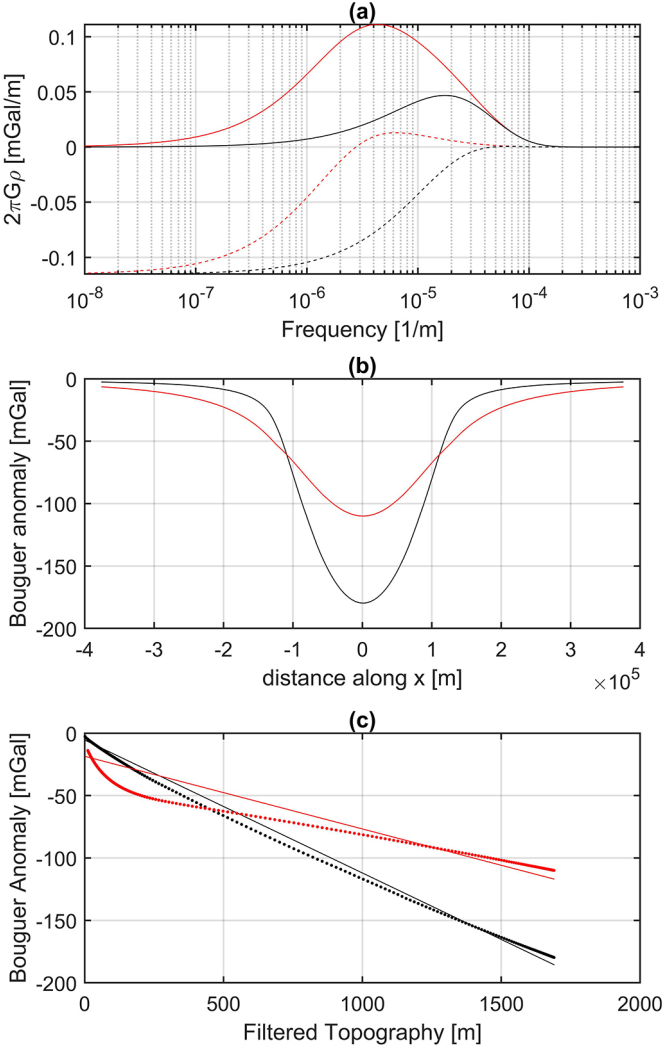
(a)
0.1
0.05
0
-0.05
-0.1
$2\pi G\rho$ [mGal/m]
10^{-8}
10^{-7}
10^{-6}
10^{-5}
10^{-4}
10^{-3}
Frequency [1/m]
(b)
0
-50
-100
-150
-200
Bouguer anomaly [mGal]
-4
-3
-2
-1
0
1
2
3
4
distance along x [m]
$\times 10^5$
(c)
0
-50
-100
-150
-200
Bouguer Anomaly [mGal]
0
500
1000
1500
2000
Filtered Topography [m]

Figure 4

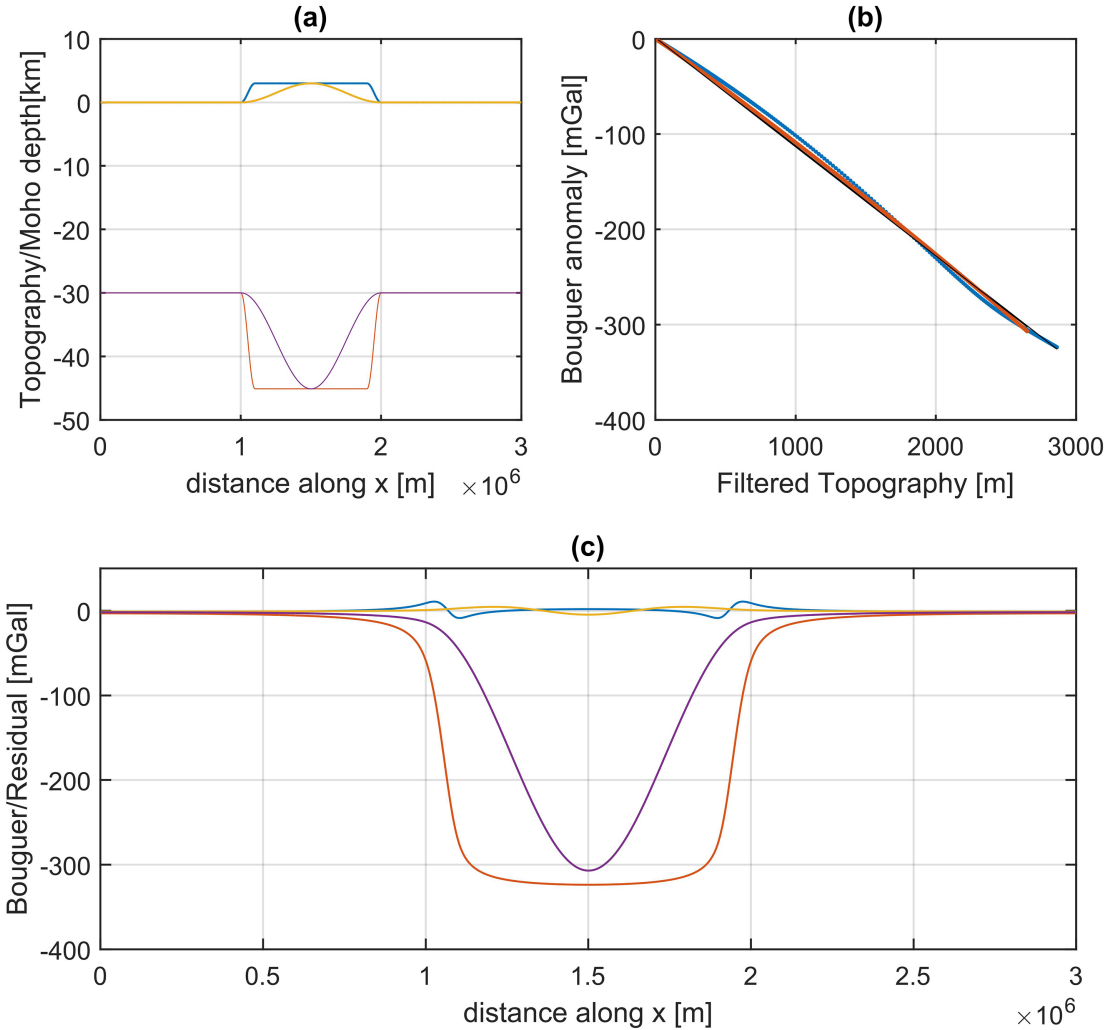
(a)
Topography/Moho depth[km]
10
0
-10
-20
-30
-40
-50
0
1
2
3
distance along x [m]
×10^6
(b)
Bouguer anomaly [mGal]
0
-100
-200
-300
-400
0
1000
2000
3000
Filtered Topography [m]
(c)
Bouguer/Residual [mGal]
0
-100
-200
-300
-400
0
0.5
1
1.5
2
2.5
3
distance along x [m]
×10^6

Figure 5

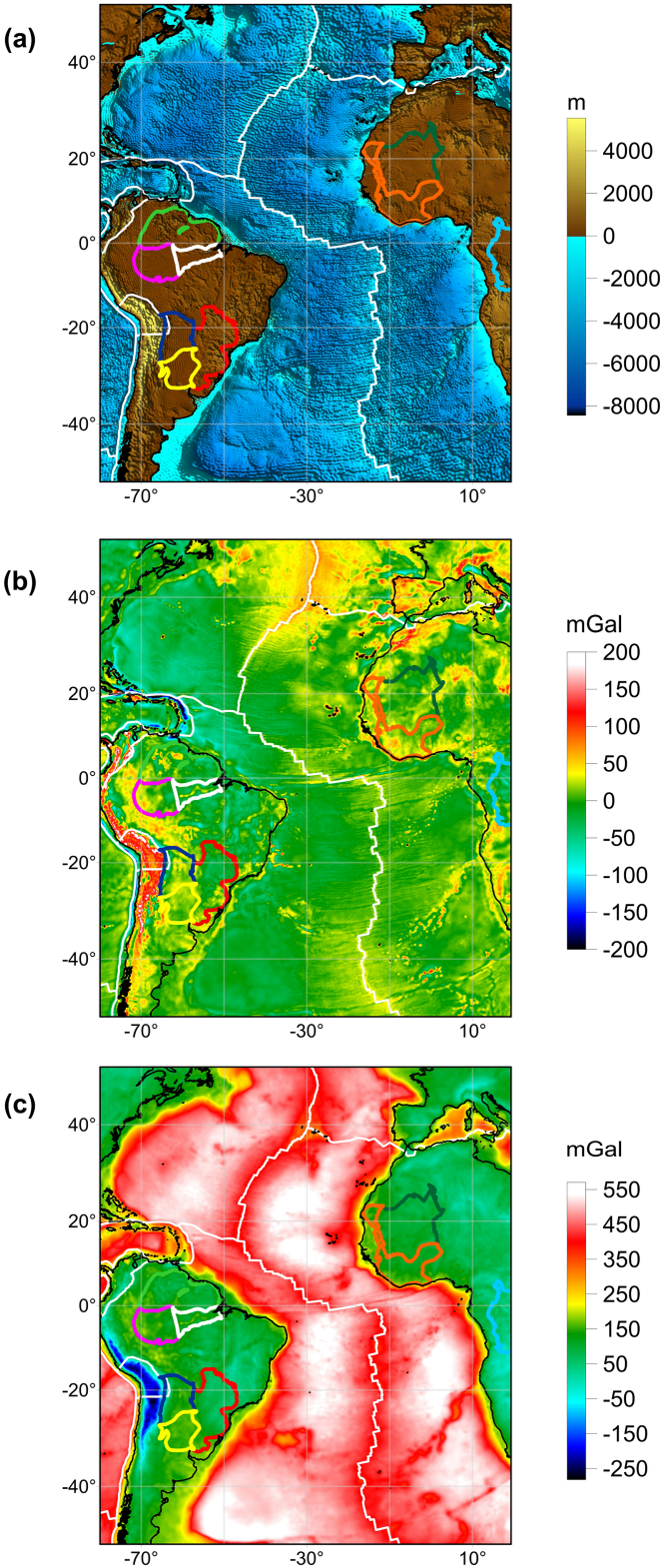
(a)
40°
20°
0°
-20°
-40°
-70°
-30°
10°
m
4000
2000
0
-2000
-4000
-6000
-8000
(b)
40°
20°
0°
-20°
-40°
-70°
-30°
10°
mGal
200
150
100
50
0
-50
-100
-150
-200
(c)
40°
20°
0°
-20°
-40°
-70°
-30°
10°
mGal
550
450
350
250
150
50
-50
-150
-250

Figure 6

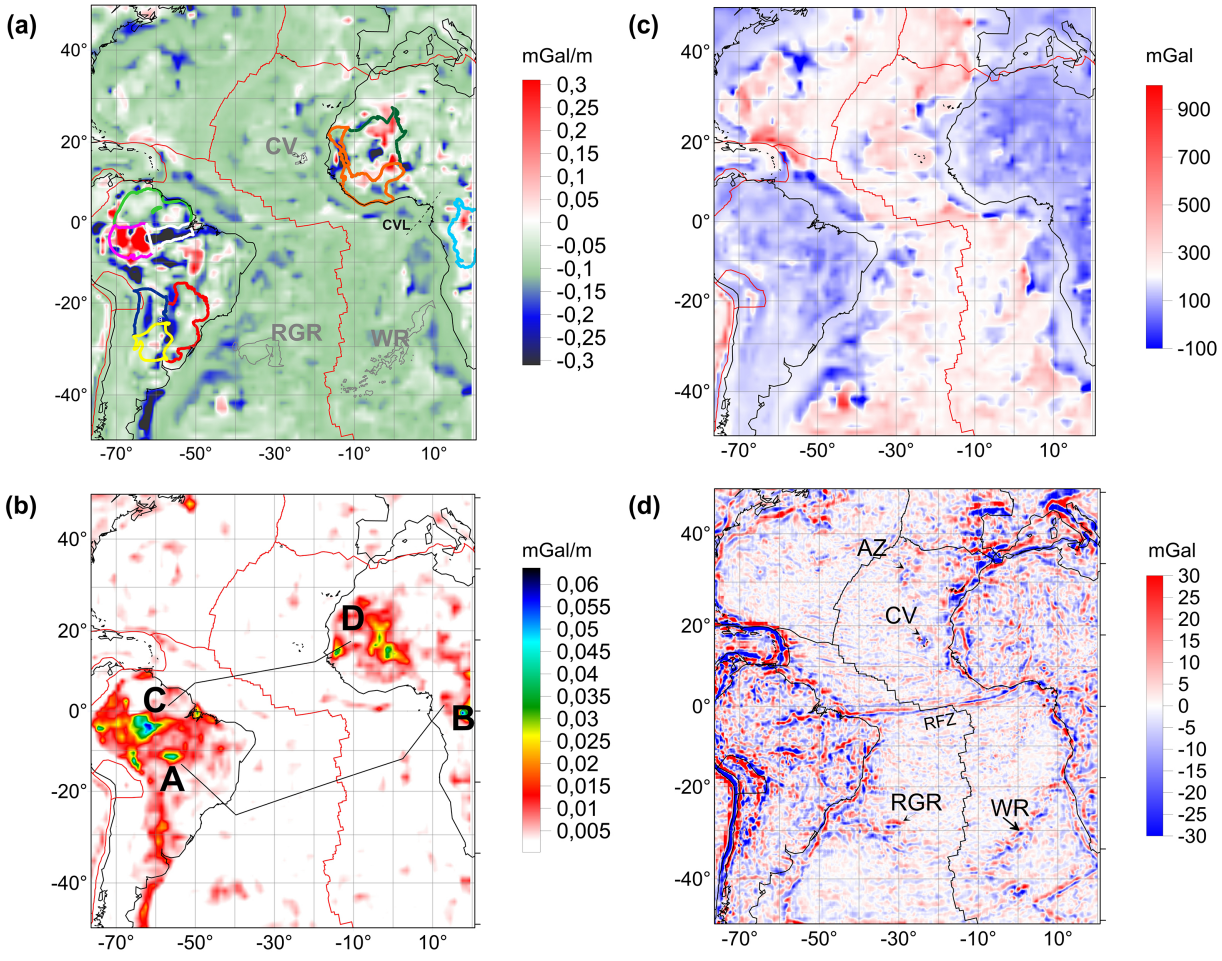
(a)
mGal/m
0,3
0,25
0,2
0,15
0,1
0,05
0
-0,05
-0,1
-0,15
-0,2
-0,25
-0,3
CV
CVL
RGR
WR
40°
20°
0°
-20°
-40°
-70°
-50°
-30°
-10°
10°
(b)
mGal/m
0,06
0,055
0,05
0,045
0,04
0,035
0,03
0,025
0,02
0,015
0,01
0,005
A
B
C
D
(c)
mGal
900
700
500
300
100
-100
(d)
mGal
30
25
20
15
10
5
0
-5
-10
-15
-20
-25
-30
AZ
CV
RFZ
RGR
WR

Figure 7

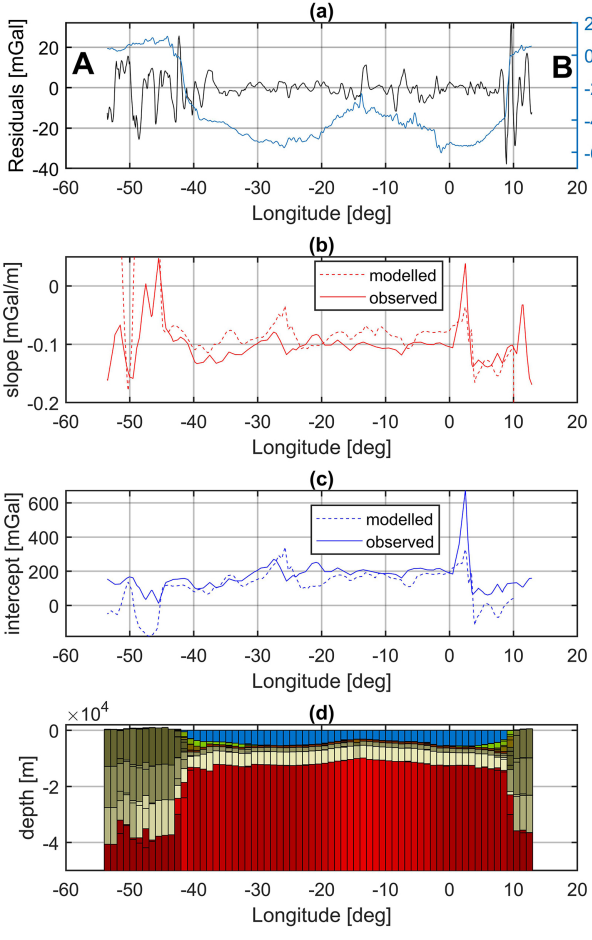
(a)
A
B
Residuals [mGal]
Topography [m]
Longitude [deg]
(b)
modelled
observed
slope [mGal/m]
Longitude [deg]
(c)
modelled
observed
intercept [mGal]
Longitude [deg]
(d)
×10^4
depth [m]
Longitude [deg]

Figure 8

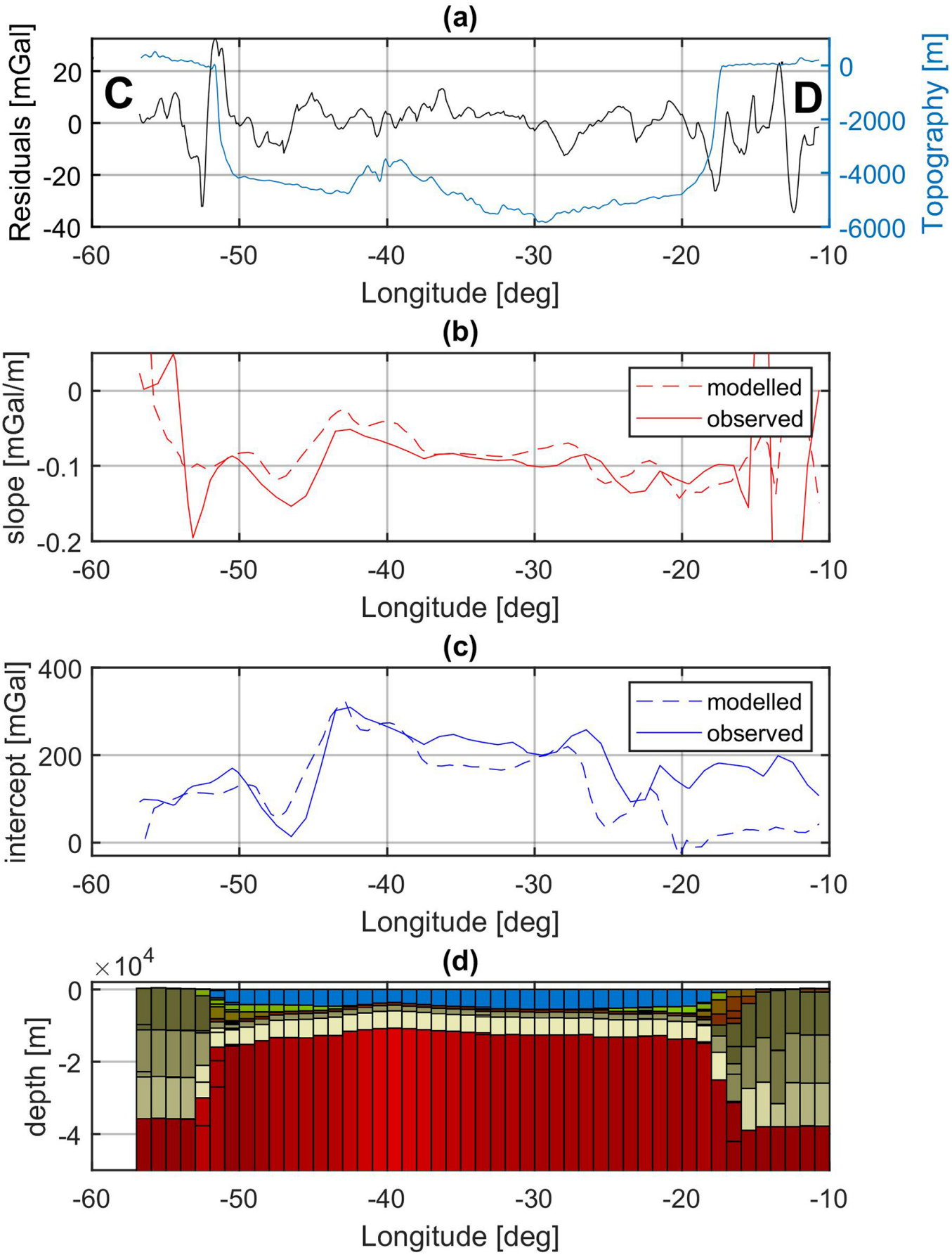
(a)
Residuals [mGal]
Topography [m]
C
D
20
0
-20
-40
0
-2000
-4000
-6000
-60
-50
-40
-30
-20
-10
Longitude [deg]
(b)
slope [mGal/m]
0
-0.1
-0.2
modelled
observed
Longitude [deg]
(c)
intercept [mGal]
400
200
0
modelled
observed
Longitude [deg]
(d)
×10^4
depth [m]
0
-2
-4
Longitude [deg]

Figure 9

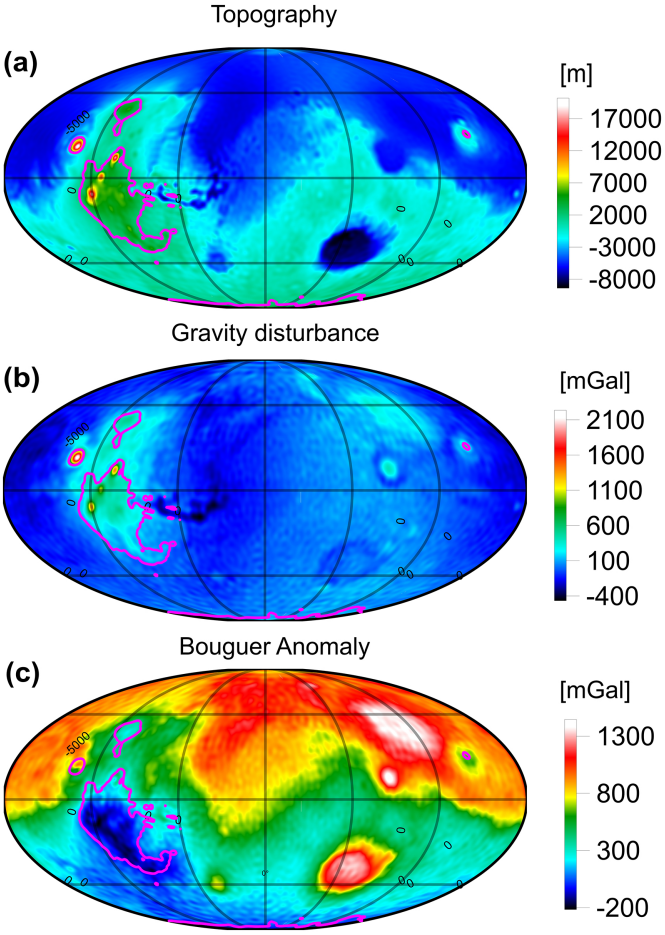
Topography
(a)
[m]
17000
12000
7000
2000
-3000
-8000
-5000
0
Gravity disturbance
(b)
[mGal]
2100
1600
1100
600
100
-400
-5000
0
Bouguer Anomaly
(c)
[mGal]
1300
800
300
-200
-5000
0

Figure 10

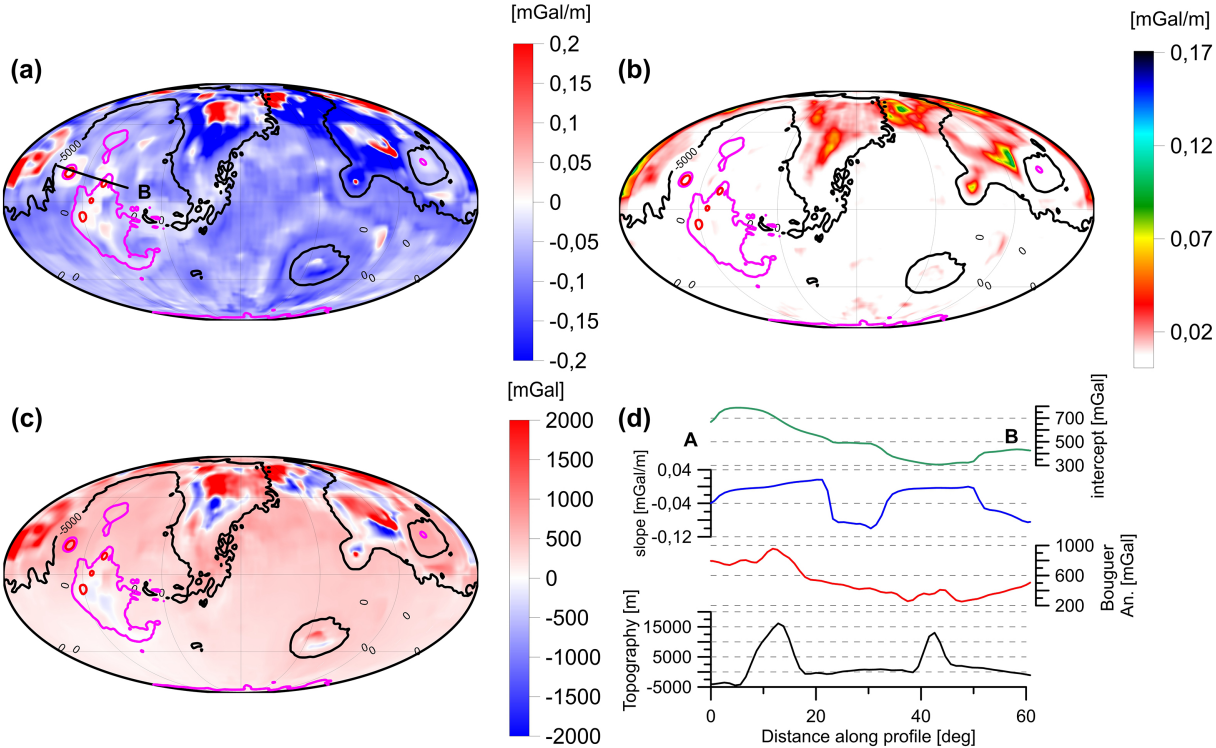
(a)
B
-5000
0
[mGal/m]
0,2
0,15
0,1
0,05
0
-0,05
-0,1
-0,15
-0,2
(b)
[mGal/m]
0,17
0,12
0,07
0,02
(c)
[mGal]
2000
1500
1000
500
0
-500
-1000
-1500
-2000
(d)
A
B
intercept [mGal]
700
500
300
slope [mGal/m]
0,04
-0,04
-0,12
Bouguer An. [mGal]
1000
600
200
Topography [m]
15000
5000
-5000
0
20
40
60
Distance along profile [deg]

Figure 11

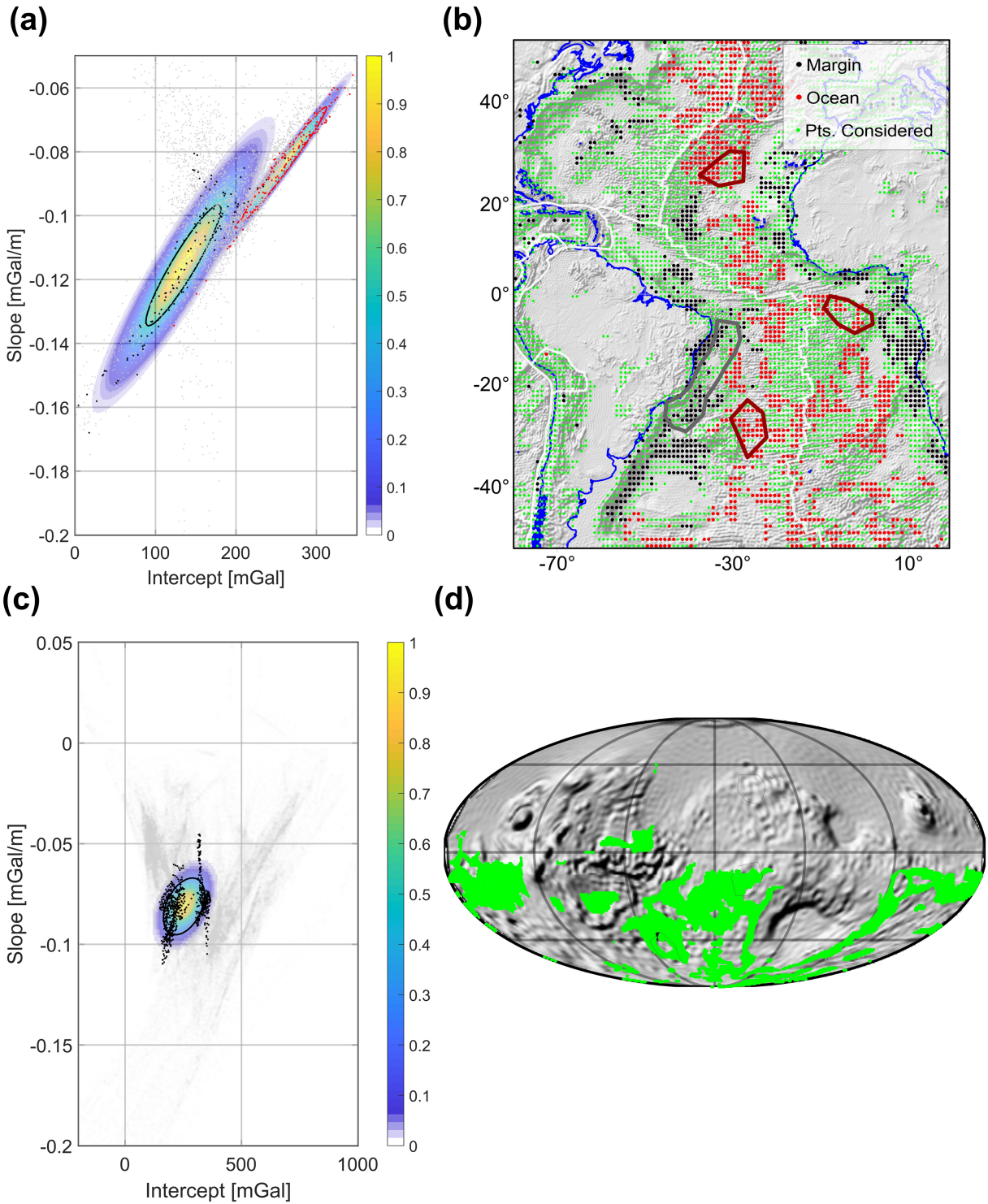
(a)
Slope [mGal/m]
Intercept [mGal]
(b)
Margin
Ocean
Pts. Considered
(c)
Slope [mGal/m]
Intercept [mGal]
(d)

Figure 12